Master's Theses (2009 -)   Dissertations, Theses, and Professional Projects

Numerical modeling of Hemodynamics in the thoracic aorta and alterations by Dacron patch treatment of Aortic Coarctation

Ronak Jashwant Dholakia
Marquette University

NUMERICAL MODELING OF HEMODYNAMICS IN THE THORACIC AORTA AND ALTERATIONS BY DACRON PATCH TREATMENT OF AORTIC COARCTATION

By

Ronak J. Dholakia, B.E.

A Thesis submitted to the Faculty of the Graduate School,
Marquette University,
in Partial Fulfillment of the Requirements for the
Degree of Master of Biomedical Engineering

Milwaukee, Wisconsin

December 2009

ABSTRACT

NUMERICAL MODELING OF HEMODYNAMICS IN THE THORACIC AORTA AND ALTERATIONS BY DACRON PATCH TREATMENT OF AORTIC COARCTATION

Ronak J. Dholakia, B.E.

Marquette University, 2009

Coarctation of the aorta (CoA) is a major congenital heart disease, characterized by a severe stenosis of the proximal descending thoracic aorta. Traditionally, surgery has been the treatment of choice for CoA. Dacron patch aortoplasty gained increased popularity after its introduction in the mid-twentieth century due to its advantages over other surgical treatment methods available at the time. A major complication with Dacron patch aortoplasty has been the formation of late aneurysm with as much as 51% incidence reported in follow up studies. The change in aortic morphology and formation of aneurysms after Dacron patch surgery could lead to local adverse changes in hemodynamic conditions which have been correlated to long term morbidity. No study to date has investigated the local hemodynamics in the human thoracic aorta and the alterations occurring in thoracic aorta of Dacron patients in detail. Computational fluid dynamics (CFD) can be used to elucidate local hemodynamics in the thoracic aorta of Normal subjects and surgically treated CoA patients. We tested the hypothesis that Dacron patch aortoplasty causes alterations in vessel wall geometry and hemodynamic indices in the thoracic aorta of CoA patients.

Patient specific CFD models were constructed for six Normal, and six age and gender matched Dacron patients. CFD simulations were performed with physiologic boundary conditions to quantify hemodynamic indices. Localized quantification of simulation results for time-averaged wall shear stress (TAWSS) and oscillatory shear index (OSI) was conducted to obtain axial and circumferential plots at various spatial locations in the thoracic aorta.

Velocity streamlines and vectors quantified from simulation results for Normal subjects were similar to the flow patterns demonstrated previously using medical imaging techniques. Spatial representations of instantaneous and time-averaged WSS as well as OSI were reflective of these velocity results. Alterations in patterns of velocity streamlines, vectors, TAWSS and OSI were observed for Dacron patients with respect to Normal subjects. Altered axial and circumferential patterns of TAWSS and OSI were also demonstrated for Dacron patients by localized quantification. These results may ultimately facilitate greater understanding if sites of long-term morbidity in Dacron patients correspond with these hemodynamic alterations during follow-up.

ACKNOWLEDGMENTS

Ronak J. Dholakia, B.E.

from undergraduate days including Jimit Doshi, Bhairav Mehta, Aniruddh Nayak, Amit

Meghani, Sankhesh Jhaveri, Alay Bhayani, and Neerav Shah.

TABLE OF CONTENTS

LIST OF TABLES

LIST OF FIGURES

Chapter 1: Introduction

1.1 Coarctation of the aorta

Congenital heart disease affects more than 32,000 infants per year in the US (i.e. about 1 in every 125-130 births) and 8-10% of these children are born with coarctation of the aorta (CoA) (Michael Madrzak 2008). CoA is more common in males than in females (2:1 ratio) and about 30% of the patients with the chromosomal disorder Turner Syndrome have CoA (Park 2003).

CoA is characterized by a severe stenosis of the proximal descending aorta. The stenosis is typically located at the aortic isthmus opposite the ductus arteriosus and just distal to the origin of the left subclavian artery. Figure 1 shows pre ductal, ductal and post ductal, the three possible types of CoA (May 2005). Post ductal CoA is the most common. CoA also commonly presents with other cardiovascular defects including ventricular septal defect, varying degrees of aortic arch hypoplasia, and hypoplastic left heart syndrome. It is estimated that up to 85 % of the patients with CoA have bicuspid aortic valve (Nichols DG 2006).
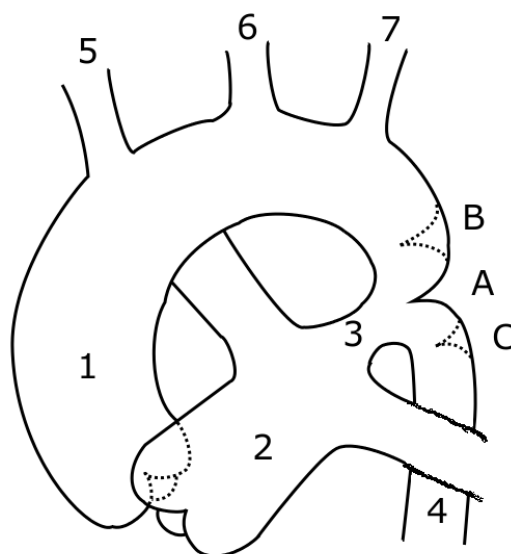
Figure 1. Schematic diagram of locations where CoA may occur, relative to the ductus arteriosus (location 3): A = Ductal coarctation, B = Pre-ductal coarctation, C = post-ductal coarctation. Other numbers indicate vascular regions of interest pertinent to the current investigation including 1 = ascending aorta, 2 = pulmonary artery, 4 = descending aorta, 5 = innominate artery, 6 = left common carotid artery and 7 = left subclavian artery. Adapted from Wikimedia Commons.

The most common hypothesis as to how CoA forms involves the ductus arteriosus

and its role as a shunt connecting the pulmonary artery to the transverse aortic arch

(Rubin 2008). In utero, the fetus receives oxygenated blood from its mother and, thus, the

right ventricle shunts blood through the ductus arteriosus to the descending aorta and

systemic circulation where the downstream resistance is low, rather than to the

pulmonary circulation where the resistance is high. After birth, systemic resistance

increases substantially while pulmonary resistance decreases. It is thought that this causes

cells lining the ductus arteriosus that have a contractile phenotype sensitive to oxygen

concentration to experience elevated oxygen saturation and thus restrict the ductus

arteriosus. Researchers have suggested an anomalous presence of some of these cells in

the descending thoracic aorta may account for CoA. A secondary hypothesis focuses on

the vicinity of the ductus arteriosus where flow may be reduced in utero, but this is a less

likely culprit for CoA since nearly all fetuses share this occurrence and yet CoA is only

present in several thousand births annually.

1.2 Associated effects

Associated anomalies such as ventricular septal defect, aortic and mitral valve

abnormalities, transverse arch hypoplasia and hypoplastic left heart syndrome may be

more frequent in infants with CoA and blood flow from the ascending aorta to the

descending aorta may subsequently be reduced. As a result, a blood pressure gradient

may develop between the proximal and distal areas of the thoracic aorta. Associated

abnormalities in asymptomatic and symptomatic infants with CoA are shown in Figure 2.

Development of collateral circulation between proximal and distal aorta is common in

older patients, therefore, blood pressure gradient may not exist in these older patients.

The Collateralization is usually not sufficient to deliver blood flow in infants, thus, when

the ductus closes they become symptomatic (Park 2003).
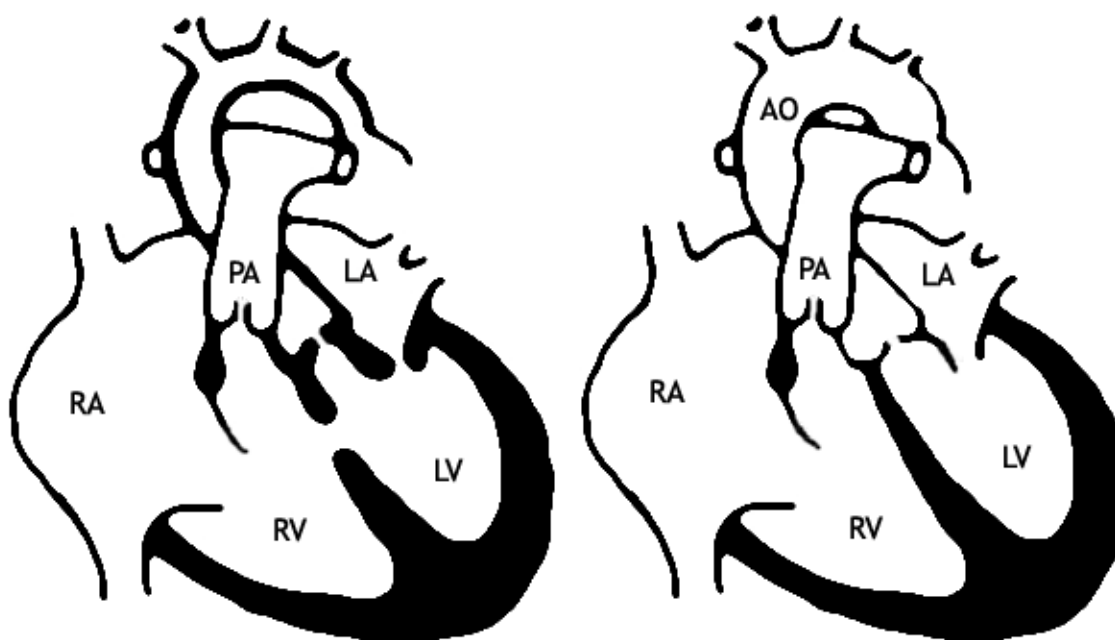
Figure 2. Symptomatic CoA (left) with associated anomalies including ventricular septal defect, aortic and mitral valve abnormalities and transverse arch hypoplasia shown with heavy lines, and asymptomatic CoA (right) with a stenosis opposite to the ductus arteriosis and no associated abnormalities. AO = aorta, LA = left atrium, LV = left ventricle, PA = pulmonary artery, RA = right atrium, RV = right ventricle. Adapted from (Park 2003)

1.3 Surgical Repair

Corrective surgery has been the treatment of choice for CoA (Schuster and Gross 1962). Resection and end-to-end anastomosis, left subclavian flap aortoplasty, and patch aortoplasty have been the three major surgical methods for CoA in infants with the latter two techniques used less often in the modern era. Figure 3 shows the various methods of CoA repair. Resection and end-to-end anastomosis involves removal of the CoA segment and suturing of the proximal to the distal aorta. Subclavian flap aortoplasty involves use of the left subclavian artery to reconstruct the narrowed aortic arch, sacrificing the left subclavian artery. In patch aortoplasty, the coarctation segment is incised longitudinally up to the left subclavian artery. An elliptical synthetic patch is then inserted between the two longitudinal sides of the CoA segment to expand the lumen diameter (May 2005; Michael Madrzak 2008; Park 2003; Vossschulte 1957)
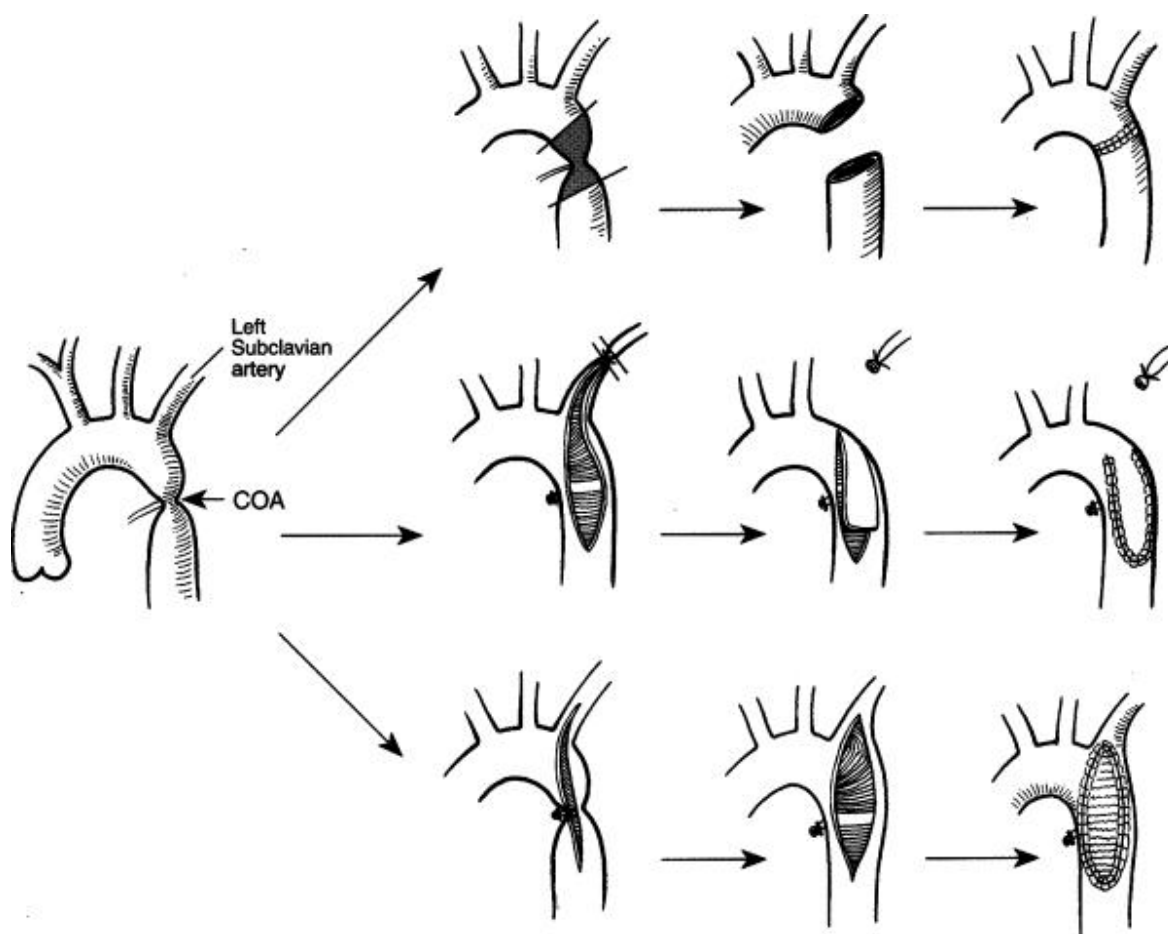
Figure 3. Schematic representations of corrective surgical repair methods for CoA. Top - resection and end-to-end anastomosis with the coarctation segment removed and the proximal and distal aorta sutured together. Middle - left subclavian aortoplasty where the distal portion of the left subclavian artery is ligated and the proximal part is sutured between the longitudinal ends of the coarctation segment. Bottom - Dacron patch aortoplasty where an incision is made longitudinally along the coarctation segment and the patch is sutured between the two ends to expand the lumen diameter. Adapted from (May 2005)

As compared to resection with end-to-end anastomosis, Dacron patch aortoplasty gained popularity, in the 1960s because it eliminates the need for circumferential suture lines and does not disrupt the intercostals arteries originating from the descending thoracic aorta (Vossschulte 1957). There are reports documenting decreased rates of

recoarctation as a result (Omeje IC 2004). This technique is also favorable since perfusion to the left arm is not compromised as compared to subclavian flap aortoplasty. Dacron patch aortoplasty is also a relatively simpler surgical procedure (Omeje IC 2004; Vossschulte 1957).

1.4 Late Aneurysm formation

Unfortunately, surgical repair of CoA has been associated with cardiovascular mortality and morbidity. Coronary artery disease, heart failure, cerebrovascular incidents and ruptured aortic aneurysms have been the main causes of death in CoA patients treated surgically (Cohen et al. 1989; Hoimyr et al. 2006; Rees et al. 1989). Late aneurysm formation, a more serious complication, has been observed, in particular, with those patients previously undergoing surgical treatment by patch aortoplasty (Hehrlein et al. 1986; Parks et al. 1995; Roth et al. 2002; Wilson et al. 1997). A long-term study by Parks et al. reported 51% incidence of late aneurysm formation in patients who underwent Dacron patch aortoplasty for CoA (Parks et al. 1995). Rupture of these aneursyms can prove fatal in patients (Hehrlein et al. 1986; Roth et al. 2002; Wilson et al. 1997). Figure 4 shows presence of an aneurysm in a 25 year old male patient treated for CoA with Dacron patch aortoplasty. Recognition of late aneurysm formation related to the Dacron patch in CoA patients has caused Dacron patch aortoplasty to fall out favor; as surgeons developed techniques to have a leveled suture line in end-to-end repair.

A comparative study between CoA patients treated with patch aortoplasty and end-to-end anastomosis revealed formation of aneurysms and increased hypertension in

patch aortoplasty patients (Walhout et al. 2003). An experimental study in canines compared results of Dacron patch aortoplasty with polytetrafluoroethylene (PTFE) patch aortoplasty. Occurrence of aneurysms was higher in the Dacron group than in the PTFE group (DeSanto et al. 1987). The location of aneurysm formation was always opposite the patch. The study also revealed that formation of aneurysms was caused by extensive resection of the intima. Pseudo-aneurysms have also been reported (DeSanto et al. 1987; Hehrlein et al. 1986; Heikkinen et al. 1990; Nagano et al. 2007; Parks et al. 1995; Roth et al. 2002; Walhout et al. 2003; Wilson et al. 1997) due to partial transmural leakage of blood from the vessel in the absence of complete dissection. This may occur due to suture-line failure at the proximal or distal anastomosis or breakage of the Dacron fibers.

Formation of true aneurysms is a more serious and concerning problem, as it involves abnormal dilation and thinning of the vessel wall. Pathologic findings studied in patients with aortic rupture or aneurysm resection reveal fibrosis and necrosis of the media in the area around the Dacron patch (DeSanto et al. 1987; Hehrlein et al. 1986; Heikkinen et al. 1990; Nagano et al. 2007; Parks et al. 1995). Disruption of elastic lamellae was also observed. Endothelialization of the Dacron patch with foreign body reaction was seen with the presence of macrophages in histological findings (DeSanto et al. 1987; Hehrlein et al. 1986; Heikkinen et al. 1990; Nagano et al. 2007; Parks et al. 1995; Shi et al. 1997) .
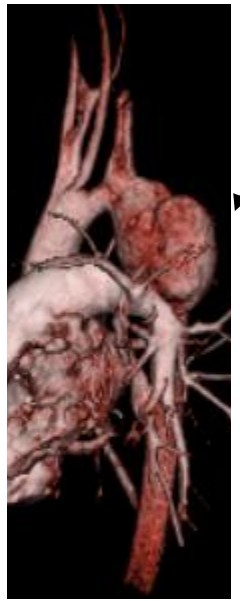
Figure 4. 3D reconstruction of magnetic resonance angiography sequences showing an aneurysm in the area of a Dacron patch repair done 22 years earlier in a 25 year old male CoA patient.

1.5 Changes in hemodynamics and vascular biomechanics after surgery for CoA.

It is extremely important to note that although simulations conducted for the current investigation utilize rigid walls, understanding of changes in vascular biomechanics resulting from the Dacron patch treatment of CoA is paramount for appreciating the local hemodynamic alterations quantified below.

Vascular impedance can be described as the pulsatile resistance to blood flow and further classified into terminal, characteristic, longitudinal and transverse impedance. These represent the impedance from the peripheral vasculature distal to the local blood vessel, total impedance of the local vasculature without any wave reflection from the distal vasculature, the relation between pressure drop and flow for a uniform segment of

blood, and the relation between transmural pressure drop and difference due to change in diameter, respectively (Westerhof, Stergiopulos, and Noble 2005). Appleyard and Sauvage in their study have shown that vessel impedance is altered after arterial replacement with a synthetic vascular prosthesis (Appleyard and Sauvage 1986). In the same study, characteristic impedance computed from longitudinal and transverse impedance was found to increase progressively in magnitude with frequency after arterial replacement with Dacron prosthesis.

Murgo et al (Murgo et al. 1981) studied the effects of exercise on aortic input impedance and pressure waveforms in normal humans. Exercise was found to cause an increase in characteristic impedance and decrease in peripheral resistance. Reductions in wave reflection are anticipated during exercise, as vessels vasodilate and more of the pressure pulse is transmitted, due to an increase in vessel caliber. Kim et al. compared exercise hemodynamics in patients with Dacron grafts and control subjects (Kim et al. 1995). They observed a 29% rise in characteristic impedance and a 21% decrease in total systemic arterial compliance in Dacron grafts during exercise. Changes in control subjects from rest to exercise were not as pronounced, underscoring increased vascular stiffness in patients with Dacron grafts. In their study, Kim et al reported reductions in wave reflection during exercise were less pronounced in Dacron grafts as compared to control subjects. Thus, the authors postulated that CoA patients treated by Dacron patch have a reduction in power transfer efficiency in the arterial system due to presence of less compliant Dacron grafts (Kim et al. 1995). In a related study, simulation of arterial hemodynamics after partial replacement of the aorta with synthetic graft material

revealed alterations in aortic input impedance and hemodynamics, whereas the peripheral resistance remained unaltered (Bauernschmitt et al. 1999).

McGiffin et al. developed a two-dimensional (2D) non-linear mathematical model and a three-dimensional (3D) finite element model to measure aortic wall stress after repair with PTFE synthetic patch material (McGiffin et al. 1992). They observed high wall stress on the synthetic patch and the wall opposite the patch location. High wall stress was not observed in areas away from the synthetic patch. The authors therefore believe post-stenotic wall thinning and high wall stress on the aortic wall were responsible for disintegration of the medial layer of the aorta and subsequent formation of true aneurysms. Smaill et al. also studied the changes in wall geometry and strain resulting from the introduction of a synthetic patch (Smaill et al. 2000). They observed decreases in circumferential curvature and substantial increases in wall strain adjacent to the patch. These variations in wall strain and local vascular geometry, when combined with the resulting blood flow alterations, may also contribute to disruption of the medial layer in the aortic wall.

In 1988, a study by Ala-Kulju et al. reported a 32% incidence of aneurysm formation in CoA patients treated with Dacron patch aortoplasty and suggested that long term follow-up would find a further increase (Ala-Kulju and Heikkinen 1989). In 1995, Parks et al. reported a 51% incidence of aneurysm formation in their long-term follow up study as mentioned above (Parks et al. 1995). These studies prompted widespread abandonment of the Dacron patch as a synthetic material used for CoA repair around the mid-to-late 90s.

1.6 Thoracic aorta blood flow patterns revealed by medical imaging

Multidirectional analysis has been used to study flow patterns in the human thoracic aorta (Frydrychowicz et al. 2008; Kilner et al. 1993; Wentzel et al. 2005). Kilner et al found a right handed helical flow pattern in the upper aortic arch in late systole and variation in this normal helical flow pattern depends on the arch geometry and curvature. Figure 5 shows the schematic representations of the findings by Kilner et al at three different time intervals over the cardiac cycle.
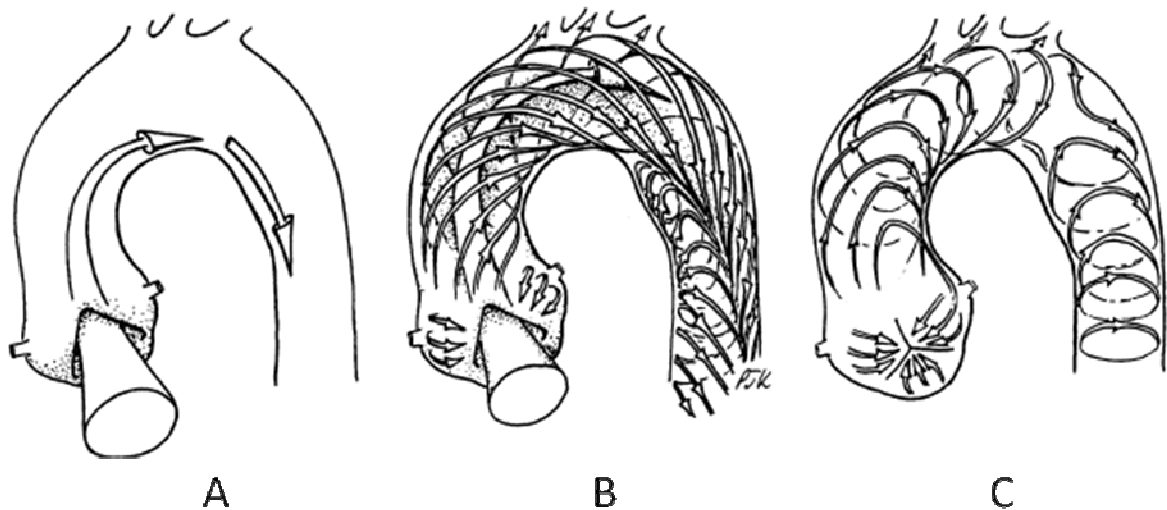
Figure 5. Schematic drawings delineating flow patterns in the aortic arch during early systole (A, highest axial velocities along the inner curvature), mid-to-late systole (B, development of secondary helical flow and highest axial velocities along the outer curvature of the aorta and some separation of flow from the inner arch), and end systole (C, re-circulating and rotational flow). Adapted from (Kilner et al. 1993)

Frydrychowicz et al performed multidirectional flow analysis of aneurysms developed after surgical repair of CoA. They observed increased flow velocities through the transverse arch and abnormal velocity patterns in the aneurysm. Decreased wall shear stress (WSS) and increased oscillatory shear index (OSI) were seen in the aneurysms compared to the ascending aorta and the transverse arch.

1.7 Statement of Hypothesis

Most aneurysms are formed opposite the synthetic patch location, but precise factors causing aneurysm formation at the site of the aortoplasty still remain unclear (von Kodolitsch et al. 2002). However, Dacron patch aortoplasty is no longer implemented for treatment of CoA due to the reported high incidence of aneurysms as mentioned above. Thus, a causal relationship between altered hemodynamics and the likelihood of aneurysm formation or rupture may not be possible and is, perhaps, not the most important question for this patient population, many of whom were treated decades ago. Instead, it is important to understand the ramifications and severity of altered hemodynamics due to aneurysms and current aortic morphology as well as their impact on indices known to correlate with long-term morbidity. To date, detailed quantification of local hemodynamics and indices of wall shear stress have not been conducted in the normal thoracic aorta or applied to Dacron patch patients to quantify the severity and sites of alterations. These local alterations can now be quantified using computational fluid dynamics (CFD) (Steinman and Taylor 2005). Further investigation into the hemodynamic basis of morbidity and treatment outcomes for patients is particularly

interesting when we consider recent advancements in computational modeling tools (Figueroa et al. 2006; Vignon-Clementel et al. 2006; Wilson et al. 2001). Patient specific anatomy can now be extracted, and geometrically representative computational models of the vasculature can be created, using information obtained during a routine clinical imaging session (Pekkan et al. 2005; Socci et al. 2005). This anatomic data, in concert with other physiological data obtained during the imaging session, such as phase-contrast magnetic resonance imaging (PC-MRI) and four-extremity blood pressure (BP), can be used to create 3D, patient-specific, time-varying representations of hemodynamics throughout the cardiac cycle. These tools offer the potential to quantify hemodynamics in a 3D and temporal manner that is not possible with other modalities. This paradigm has been successfully applied to other congenital heart defects, specifically those classified as "single ventricles." In these patients, computational fluid dynamics (CFD) simulations of the Fontan procedure has led to widespread acceptance of several technical modifications demonstrated to be more energy efficient to previous surgical techniques (Pizarro and De Leval 1998). If these techniques were applied to the thoracic aorta of normal and then CoA patients, similar studies would likely provide greater understanding of long-term morbidity, offer a screening tool for identifying vascular sites for longitudinal evaluation, and potentially promote preoperative assessment of treatment options.

Therefore, the current investigation tested the hypothesis that Dacron patch aortoplasty causes alterations in vessel wall geometry, blood flow, local patterns of velocity, and indices of wall shear stress in the thoracic aorta of patients previously treated for CoA. Three specific aims were identified to test this hypothesis.

Specific aim 1: Quantify and characterize hemodynamics including local velocity profiles, temporal streamlines revealing flow patterns, TAWSS, and OSI for the thoracic aorta of Normal subjects.

Specific aim 2: Quantify and characterize hemodynamics including local velocity profiles, temporal streamlines revealing flow patterns, TAWSS, and OSI for the thoracic aorta in age and gender matched CoA patients previously treated by Dacron patch aortoplasty.

Specific aim 3: Compare the local position and severity of alterations in WSS indices within the thoracic aortas of CoA patients previously treated by Dacron patch aortoplasty with age and gender matched normal subjects to delineate the potential regions of hemodynamic susceptibility after patch correction and offer a screening tool for other corrective repairs for CoA or diseases of the thoracic aorta.

Chapter 2 Methods

2.1 Magnetic Resonance Imaging

Six patients (5 male and 1 female, mean age 29) previously treated for CoA by surgical Dacron patch aortoplasty and six Normal subjects (5 male and 1female, mean age 29) were previously imaged as part of the ongoing IRB approved protocol of John LaDisa Ph.D. and his collaborators. Primary and secondary diagnoses for the six CoA patients are provided in Table 1. Imaging sessions were performed at the Children's Hospital of Wisconsin (CoA patients) and Lucile Packard Children's Hospital at Stanford University (Normal subjects). CoA and Normal participants underwent Gadolinium-enhanced magnetic resonance angiography (MRA) using 1.5T Siemens Symhony^R and GE Signa^R MR scanners, respectively. MRA sequences consisted of a three-dimensional fast gradient echo sequence to obtain a volume of coronal slices. Slice thickness ranged from 2.0 to 2.2 mm, with 54 to 56 slices per volume. A 384 x 192 acquisition matrix (reconstructed to 384 x 256) was used with a field of view of 20 x 30 to 25 x 38 cm^2 to provide a reconstructed spatial resolution of 0.610 to 0.966 mm. Other scan parameters included repetition times (TR) of 4.3 ms, echo times (TE) of 1.3 to 1.6 ms, and a flip angle of 25°. Participants were instructed to hold their breath during the MRA data acquisition period (~10-20 seconds) when age and ability permitted.

MRA data was used to delineate the anatomy of the thoracic aorta and the innominate (IA), left and right carotid (LCCA and RCCA), and left subclavian (LSA) arteries during the construction of patient-specific CFD models.

Table 1. Primary and secondary diagnoses of the six CoA patients treated by Dacron patch aortoplasty.

Patient no	Age (years)	Gender	Primary Diagnosis	Secondary Diagnosis
1	32	Male	CoA, s/p Dacron patch repair, s/p Ao valve replacement (carbomedics)	Bicuspid Ao valve (AoV)
2	25	Male	CoA, s/p Dacron patch repair 1985	Aneurysm of descending aorta
3	33	Male	CoA, s/p Dacron patch repair	Bicuspid Ao valve with aortic regurgitation (AR)
4	33	Female	CoA, s/p Dacron patch repair	Bicuspid Ao valve
5	26	Male	CoA, s/p Dacron patch repair	Bicuspid AoV with AR
6	26	Male	CoA, s/p Dacron patch repair 1988	Bicuspid Ao valve

PCMRI sequences were performed for CoA patients in the ascending aorta slightly above the aortic root, in the descending thoracic aorta at the level of the diaphragm, and just distal to the IA, LCCA and LSA ostia. Velocity encoding (VENC) gradients were set by Margaret Samyn MD and Joseph Cava MD, PhD during clinical imaging sessions to optimize the dynamic range of the phase shift within the blood vessel of interest. The open source software Segment v1.700 (http://segment.heiberg.se) (Heiberg 2007) and cvSim^{TM} (Cardiovascular Simulation. Inc, Mountain View, CA) (Wilson et al. 2001) were used to quantify flow from PCMRI data in DICOM or 5X format for Dacron patients and Normal subjects, respectively.

Phase contrast images obtained perpendicular to each aortic location and the IA, LCCA and LSA were used to calculate time-resolved volumetric blood flow as previously described (Tang et al. 2006). Briefly, the PCMRI magnitude data was segmented using level set (Wang, Dutton, and Taylor 1999) or manual segmentation techniques to delineate the vessel lumen. Pixel velocity values within these segmentations were adjusted with a second order spatially dependent baseline correction algorithm to account for phase errors that result from gradient eddy currents and magnetic fields as seen in Figure 6 (Bernstein et al. 1998; Heiberg 2007). Instantaneous flow rates were then computed by integrating the corrected velocity values over the lumen cross sections (Pelc et al. 1992).
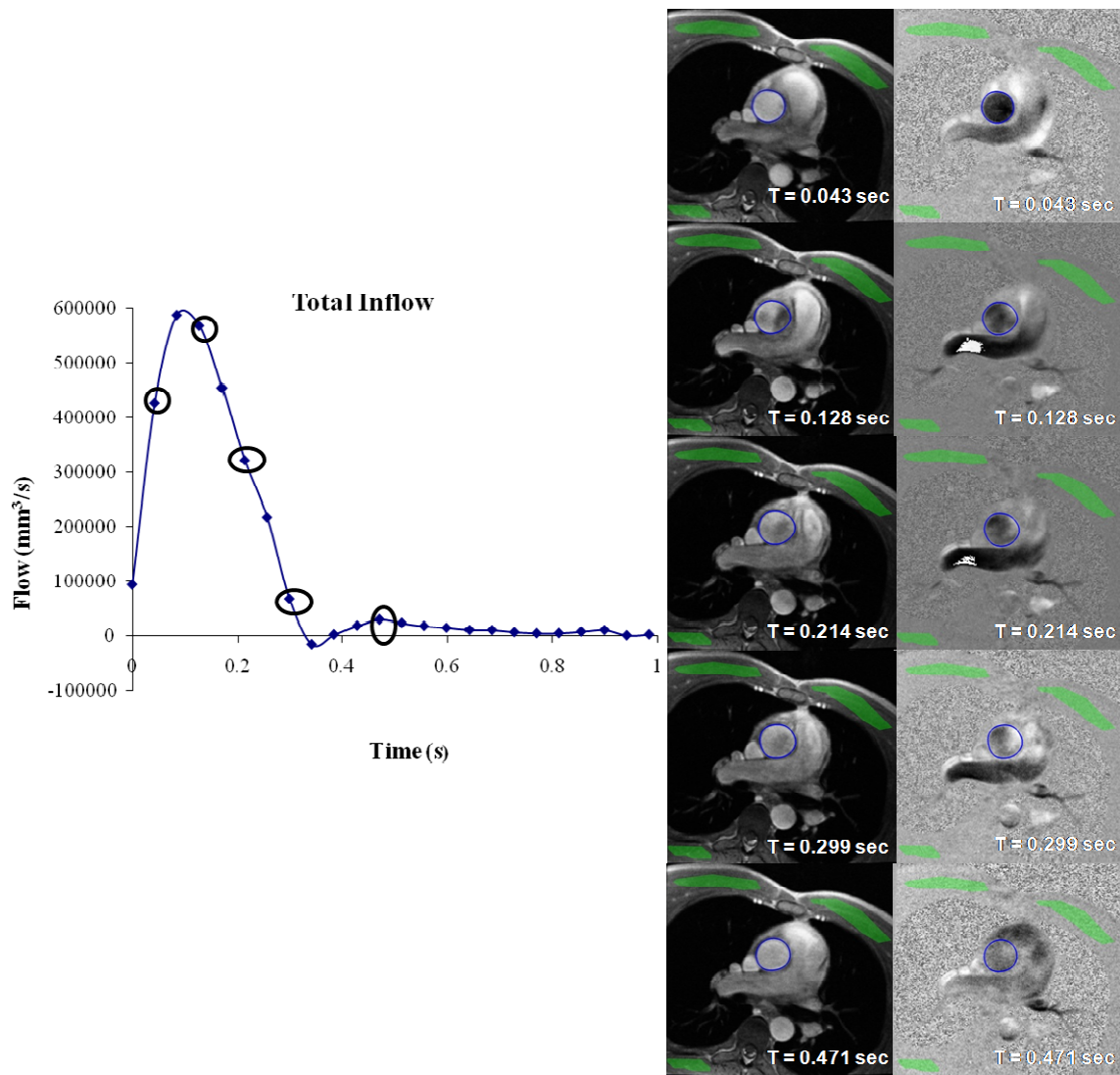
Figure 6. Magnitude images to the left and on their side the corresponding phase images for timeframes 2, 4, 6, 8 and 12 taken through the ascending aorta at the level of the pulmonary arteries just above the aortic valve in a 32 year old normal male subject and the flow waveform with these time frames circled, shown next to it. The vessel lumen becomes darker in the magnitude and phase images during the peak systole at time 0.128 sec. The phase difference is highest during acceleration in early systole at 0.043 sec (frame 2).

PCMRI sequences were only performed at the ascending aorta location for Normal subjects and were processed as described above. The distribution of blood flow to each of the branch vessels and descending aorta was estimated from a previously published relationship between the diameter and flow of the ascending aorta and the diameter and flow of branch vessels described by M.Zamir et al. (Zamir, Sinclair, and Wonnacott 1992) that was conducted using rigid casts of the lumen geometries. The geometries were obtained from two specimens of the human aortic arch obtained at autopsy from a 53 male subjects and 38 female subjects with their ages ranging from 20 to 92 years. In-vivo flow measurements were made through the rigid casts and the diameters of the branch were directly measured with calipers. If flow through the parent vessel is denoted as q_0 and its branch vessels at distal to a bifurcation are q_1 and q_2, then the flow rates for the three vessels are related by 2.1 by conservation of mass

$$q_0 = q_1 + q_2 \qquad\qquad 2.1$$

The flow and diameter of a vessel are proportional through the power law index given below as:

$$d_0^x = d_1^x + d_2^x \qquad\qquad 2.2$$

In 2.2, d_0, d_1, and d_2 denote the respective diameters of the corresponding vessels. Using these expressions, the authors determined that the relationship between q and d^x obeys a power law index of 2 for the head and neck vessels, consistent with area preservation thought to be advantageous for delivering large amounts of blood rapidly though conduit arteries.

PCMRI data was unavailable for one Normal subject (24 yo male). To circumvent this limitation, body surface area was calculated from a previously published relationship between ascending aortic cross sectional area and body surface area (Seear, Webber, and Leblanc 1994). Cardiac output was then determined using the average cardiac index for the other Normal subjects and the calculated body surface area. An inflow waveform contour for the patient was obtained by ensemble averaging PCMRI waveforms measured in healthy children (Cheng et al. 2004) and scaling the ensemble averaged waveform to match the cardiac output determined from the product of body surface area and cardiac index.

2.2 Blood pressure measurements and assumptions

Blood pressures (BP) in the upper and lower limbs of CoA patients measured using Dinamap® (GE Healthcare, Milwaukee, WI) devices are provided Table 2. Differences in BP between extremity are typically caused by wave reflection and material properties which collectively cause an increase in pulse pressure with a modest reduction in mean BP, or any local stenoses which can decrease mean BP and pulse pressure (Nichols and O'Rourke 2005). As discussed below, all CFD simulations conducted for the current investigation utilized rigid walls and thus do not include the impact of material properties. Therefore, while the BP values provided in Table 2 were useful for elucidating BP gradients and replicating these gradients in resulting simulations, upper extremity pressures in non-stenotic vessels were used for setting up boundary conditions in the current investigation. BP data was not available for Normal subjects. The age and

gender of subjects were therefore used to obtain representative normal BP values from

National Health Survey Series 11, No. 234 (Drizd, Dannenberg, and Engel 1986) which

gives mean systolic and diastolic BP values for different ages and genders. The values for

various age groups applicable to the current investigation are provided in Table 3.

Table 2. Blood pressure measurements for the six Coarctation patients treated with Dacron patch aortoplasty. Measurements in both upper limbs are included below.

Patient No	Age (years)	Gender	Left arm systolic blood pressure (mmHg)	Right arm systolic blood pressure (mmHg)	Left arm diastolic blood pressure (mmHg)	Right arm diastolic blood pressure (mmHg)	Average arm systolic blood pressure (mmHg)	Average arm diastolic blood pressure (mmHg)
1	32	Male	120	154	65	62	137	63.5
2	25	Male	112	116	80	80	114	80
3	33	Male	106	108	64	64	107	64
4	33	Female	108	112	65	64	110	64.5
5	26	Male	103	136	69	74	117.5	71.5
6	26	Male	133	157	94	84	145	89

Table 3. Blood pressure data for several age groups of normal participants obtained from Health Survey Series 11, No. 234. This data was used to assume systolic and diastolic pressure values for Normal subjects used in the current investigation depending on their age and gender

Sex	Age		
	18-24 years	25-34 years	35-44 years
	Systolic blood pressure (mmHg)		
Men	124	125	126
Women	111	112	119
	Diastolic blood pressure (mmHg)		
Men	73	76	79
Women	70	73	77

2.3 Computational model reconstruction

2.3.1 Construction of volumetric data from DICOM image slices

MRA data in DICOM image slice format was converted into .vti volume format using eFilm software® (MERGE Healthcare, Milwaukee, WI) and cvSim. The 3D volume was then visualized using volume rendering techniques and adjusting appearance settings within an open-source software project VolView (Kitware, Inc., Clifton Park, New York) to determine rendering values for scalar and gradient opacity and color mapping. The .vti volume file was then loaded in cvSim and visualized using theses parameters.

2.3.2 Model reconstruction from MRA volume data

After visualizing the volume, centerline paths were manually assigned using cvSim along each vessel lumen of interest. These paths act as the basic framework for model reconstruction. The manual assignment of paths first involved selection of starting and ending points. Depending on the length and tortuosity of the vessel of interest, a specific number of spline points were then introduced between the start and end points. These points were then fit to a spline curve typically containing 15 to 20 spline points for the aorta and fewer for branch vessels. Paths were then saved with a distinct ID number.

The vessel lumen along each path was delineated by segmenting the area of the lumen in an intensity window orthogonal to the path. Separate group files were created

for each vessel where individual segments were saved. The segments were created using the automated level set algorithm and manual segmentation techniques. Two consecutive segments were not allowed to intersect to avoid lofting issues. All 2D segments for the individual groups were then lofted along the paths to create a vessel solid and individual vessel solids were combined to create a solid model as depicted in Figure 7. Junctions between the parent vessel and the branches of the final solid model were blended to make them smooth and more reflective of physiology. The ascending aorta inlet surface was tagged as the inflow face and the descending aorta outlet surface was tagged as the outflow face. Patient-specific models constructed using the above methods for the six Normal subjects and Dacron patients are shown in Figures 8 and 9, respectively.
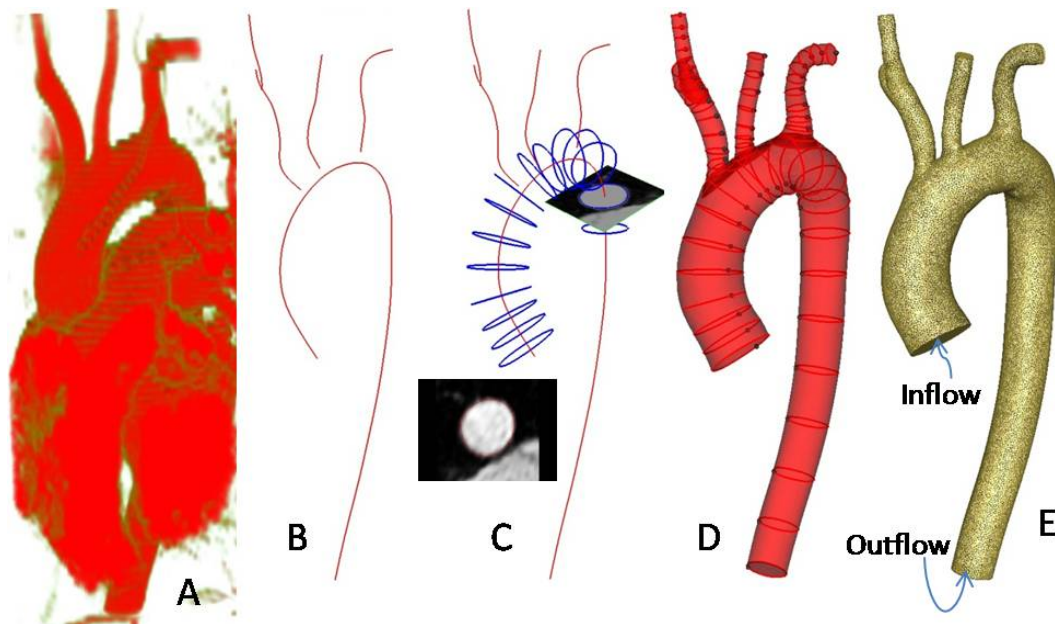
Figure 7. Creating patient specific CFD models from MRA data (A) includes finding the centerline path of each blood vessel (B), performing segmentation of the vessel lumen (C), connecting segments to form a model (D) and meshing the solid model (E). Panel E also shows the inlet and outlet faces of the computational model (5).

Figure 8. Volume rendered MRA representations for the six normal subjects (above) and their computational subject specific solid model representations (below). From left to right, patient 1 – 32 year old normal male, subject 2 – 25 year old normal male, subject 3 – 33 year old normal male, subject 4 – 33 year old normal male, subject 5 – 26 year old normal male and subject 6 – 26 year old normal female.
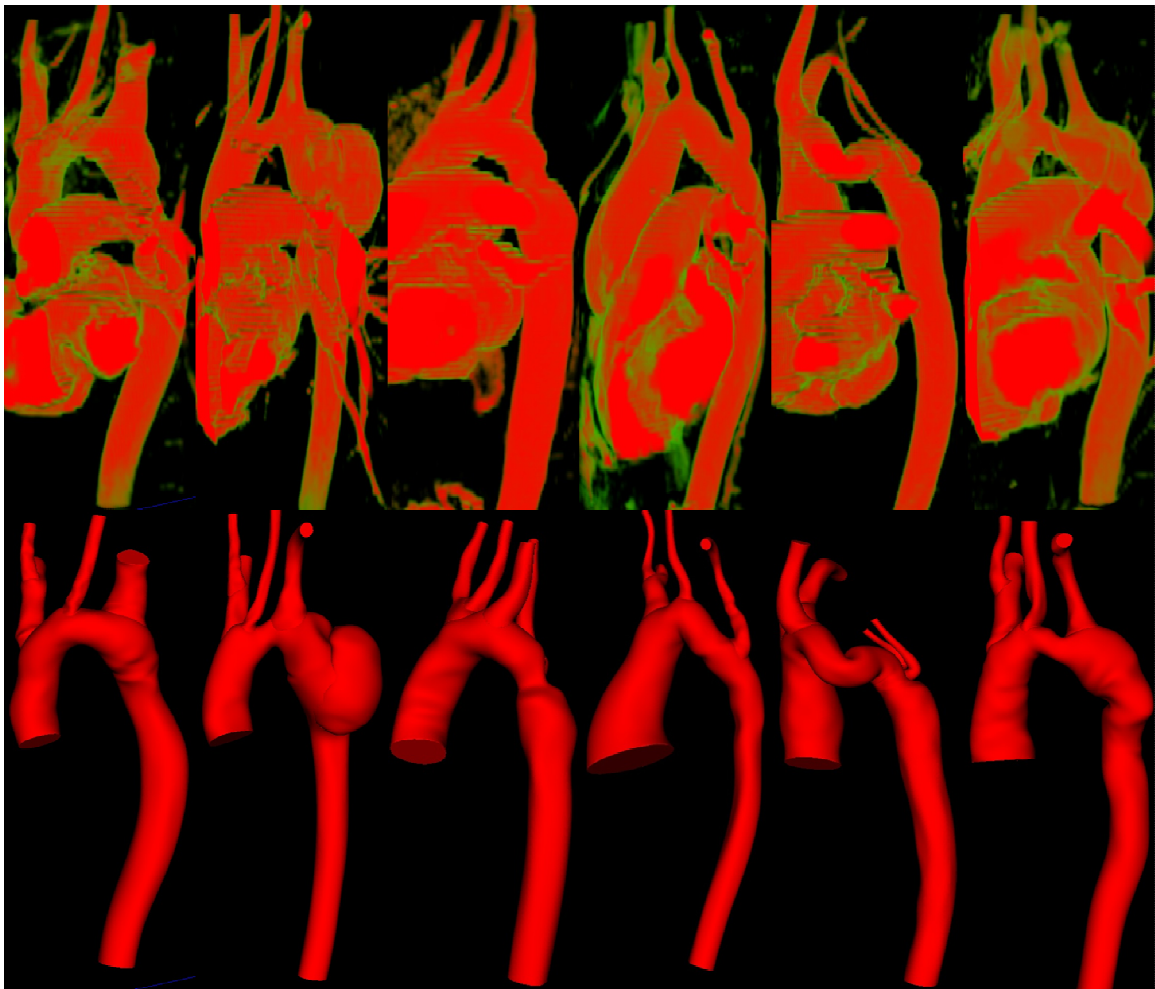
Figure 9. Volume rendered MRA representations for the six CoA patients treated with Dacron patch aortoplasty (above) and their computational subject specific solid model representations (below). Their age, gender, primary diagnoses and secondary diagnoses are given in Table 1.

2.3.3 Mesh Generation

The final solid model was then converted to a finite element mesh representing

the blood vessels of interest utilizing automated meshing techniques made possible with

the MeshSim (Simmetrix, Inc) software capabilities incorporated within cvSim.

Refinement of the mesh depends on the global max edge size defined as the maximum

length for elements within the mesh. The smaller the global max edge size, the greater the

number of elements in the mesh, but at the expense of additional computational time. A

global max edge size on the order of 1 mm was selected for the initial meshes of each

patient in order to achieve optimum mesh refinement while keeping the total number of

elements at a manageable computational level. The process of obtaining CFD results for a

single patient actually requires running several successive simulations, each of which

contains a greater number of elements in order to ensure that simulation results are

independent of the number of elements used for the simulation. The initial mesh for each

patient is isotropic, thus all elements are of the same edge size and distributions of

tetrahedral elements in all areas of the CFD model are uniform. However, after each

successive simulation an adaptive technique was employed to deposit more elements near

the luminal surface and in anatomical regions prone to flow disruption. As a result, final

CFD meshes contained >3 million locally-refined elements.

2.4 Boundary conditions and CFD Simulations

2.4.1 Generation of output files from mesh

The commercial PHASTA flow solver integrated within cvSim operates on portions of the finite element mesh by organizing it into different files that include the location of nodes, the connectivity between nodes, the boundary nodes, and the element faces to be used in prescribing boundary conditions. These files are saved after using cvSim to create the mesh from the solid model as described above and include all_exterior_faces.ebc.gz (containing element connectivity of all the exterior faces), mesh.connectivity.gz (containing element connectivity of the volumetric mesh), mesh.coordinates.gz (containing the coordinates of all the nodes of the mesh), mesh.sms (the mesh files), mesh.supre (input pre-solver file for cvSim), mesh.xadj.gz (containing the element adjacency), and inflow_mesh_face.vtk (Visualization toolkit (vtk) representation of the inflow face of the model). In addition to the above output files, a *mesh-surfaces* folder is also saved and contains the boundary element connectivity, list of nodes and vtk files for each face.

2.4.2 Inlet and outlet boundary conditions

Ascending aortic blood flow waveforms obtained from PCMRI data were prescribed on the inflow face as the inlet boundary condition. The ascending aorta PCMRI waveforms were mapped to the inlet face of the computational model using a

temporally varying parabolic flow profile. Flow waveforms obtained from the IA, LCCA and LSA and descending aorta were used, in conjunction with measured BP data, to prescribe outflow boundary conditions as discussed below. The likelihood of successfully completing a simulation (i.e. convergence) is greatly increased when pressure and velocity conditions within the problem are not forced to begin from values of zero. This is known as a "cold start" and was avoided for simulations in the current investigation by conducting steady simulations using the mean blood flow value from the ascending aortic inflow waveform of each patient. Results from the completion of these steady mean simulations utilizing mean blood flow were then applied as initial conditions for each pulsatile simulation of the entire cardiac cycle.

 Practically speaking, resistance boundary conditions were applied for mean simulations and the value for resistance at each model outlet was determined using the mechanical analogue of Ohm's law:

$$P = QR \hspace{4cm} 2.3$$

where R is the terminal resistance of the vasculature distal to the outlet face, Q is the mean physiologic flow rate through the outlet face for the branch of interest and P is the applicable mean BP value.

To replicate the physiologic influence of vessels distal to CFD model branches for pulsatile simulations, a three-element Windkessel representation was imposed at each outlet using a coupled-multidomain method as shown in Figure 10 (Vignon-Clementel et al. 2006). The three-element Windkessel representation provides a good estimate of the

arterial tree beyond model outlets (Westerhof, Stergiopulos, and Noble 2005) and can be described by three main parameters with physiologic meaning: R_c, C and R_d. R_c is the characteristic impedance representing the resistance, compliance and inertance of the proximal artery of interest, C is the arterial capacitance and represents the collective compliance of all arteries beyond a model outlet, and R_d describes the total distal resistance beyond a given outlet. The terminal resistance (R_t) for each model outlet was determined from mean BP and PCMRI flow measurements and distributed between R_c and R_d as described below. Under resting conditions, the total arterial compliance (TAC) for each patient was determined using inflow and BP measurements and assuming a R_c:R_t ratio of 6% (Laskey et al. 1990). The TAC was then distributed among outlets according to their blood flow distributions (Stergiopulos, Young, and Rogge 1992) and R_c:R_t ratios for each outlet were adjusted to between 6-10% using the pulse pressure method (O'Rourke and Safar 2005; Stergiopulos, Segers, and Westerhof 1999) thereby replicating BP values.
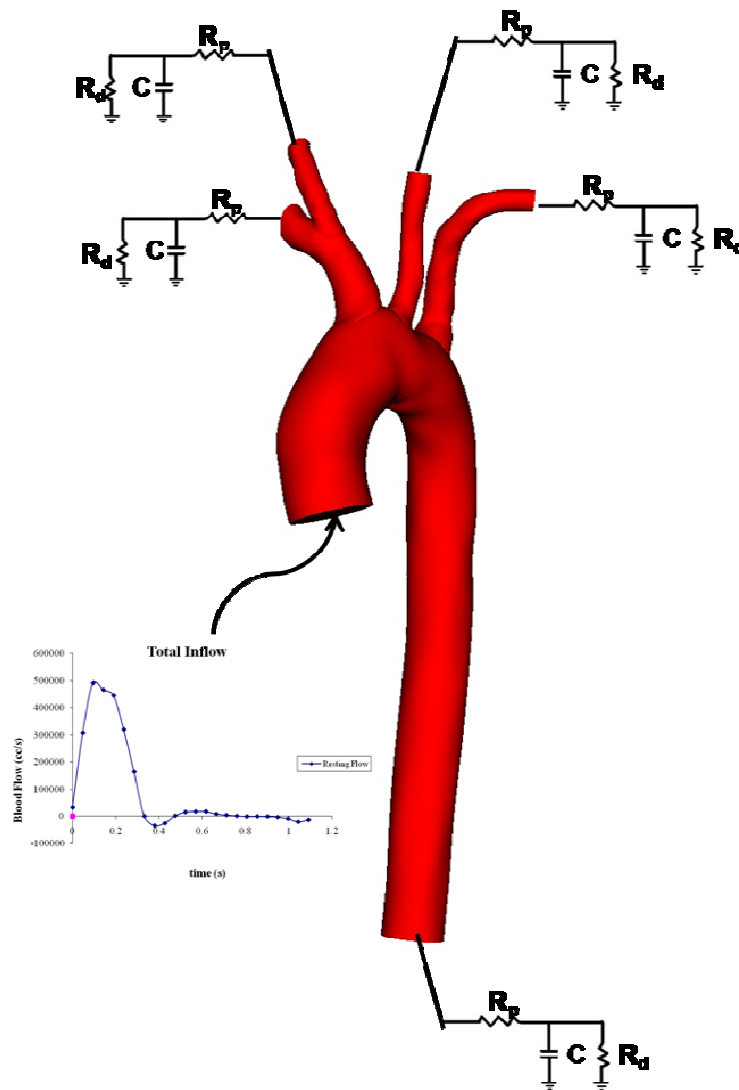
Figure 10. Boundary conditions prescribed on the inlet and outlet faces of the computational model when conducting a CFD simulation. The patient specific inflow waveform was prescribed on the inlet face and 3-element Windkessel model (RCR) representations reflective of the downstream vasculature were prescribed at model outlets.

2.4.3 CFD simulations

Simulations were performed using a novel stabilized finite element method to solve the conservation of mass (continuity) and balance of fluid momentum (Navier-Stokes) equations (Figueroa et al. 2006). Conservation of mass (continuity) equation is generally given as

{rate of mass accumulation} = {rate of mass in} – {rate of mass out}   2.4

2.11 can be expressed mathematically as

$$\frac{\partial \rho}{\partial t} + \frac{\partial(\rho u)}{\partial x} + \frac{\partial(\rho v)}{\partial y} + \frac{\partial(\rho w)}{\partial z} = 0$$ 2.5

where ρ is the density of fluid, and u, v and w are the x, y and z components of the velocity vectors u, v and w.

The Navier-Stokes equations are the governing differential equations for the motion of incompressible fluids and are developed from conservation of mass and linear momentum. They are non-linear partial differential equations given as

$$\rho\left(\frac{\partial u}{\partial t} + u\frac{\partial u}{\partial x} + v\frac{\partial u}{\partial y} + w\frac{\partial u}{\partial z}\right) = -\frac{\partial \rho}{\partial x} + \rho g_x + \mu\left(\frac{\partial^2 u}{\partial x^2} + \frac{\partial^2 u}{\partial y^2} + \frac{\partial^2 u}{\partial z^2}\right)$$ 2.6

$$\rho\left(\frac{\partial v}{\partial t} + u\frac{\partial v}{\partial x} + v\frac{\partial v}{\partial y} + w\frac{\partial v}{\partial z}\right) = -\frac{\partial \rho}{\partial y} + \rho g_y + \mu\left(\frac{\partial^2 v}{\partial x^2} + \frac{\partial^2 v}{\partial y^2} + \frac{\partial^2 v}{\partial z^2}\right)$$ 2.7

$$\rho\left(\frac{\partial w}{\partial t} + u\frac{\partial w}{\partial x} + v\frac{\partial w}{\partial y} + w\frac{\partial w}{\partial z}\right) = -\frac{\partial \rho}{\partial z} + \rho g_z + \mu\left(\frac{\partial^2 w}{\partial x^2} + \frac{\partial^2 w}{\partial y^2} + \frac{\partial^2 w}{\partial z^2}\right)$$ 2.8

where g is the acceleration due to gravity given in the *x*, *y* and *z* directions.

Blood vessels were assumed to be rigid even though they are known to be compliant. Mismatches in this mechanical property between the aorta and patch likely account for much of the geometric disparity between Dacron patients and Normal subjects observed in the current investigation. This decision was based on three factors. First, the precise location of the patch was not known for all patients since surgeries were conducted at different institutions and, in some cases, decades prior to the imaging study utilized. Second, cvSim does not currently permit the use of variable tissue properties, so implementation of deformable walls would utilize a single vascular thickness and modulus of elasticity that could introduce additional uncertainty into simulation results. Finally, the modulus of elasticity for Dacron material is substantially higher than aortic tissue of healthy younger children. When coupled with the fact that patients in the current investigation have a mean age of 29 years and their vessels are likely stiffer than those of younger patients, implementation of rigid walls offers a more reasonable assumption than a single modulus for the patch location and entire thoracic aorta. Simulations were run for 4-6 cardiac cycles until the flow rate and pressure fields yielded periodic solutions. Periodicity was assumed when the maximum error between equivalent points in successive cardiac cycles for pressure and flow were <1 mmHg and 1 mm^3/s, respectively. A constant value of 1.06 g/cm^3 was used for all patients for the density of blood. A Newtonian fluid assumption with a common viscosity of 4 cP was also used for all patients. A Newtonian fluid assumption is valid given the shear rates for the thoracic aorta and its branches, and the value is reasonable since rheological data was not available for all patients and subjects in the current investigation.

Wall shear stress is the tangential force per unit area exerted by the fluid on the vessel walls and given as

$$\tau_w = \mu \gamma_w \qquad \text{2.9}$$

where, μ is the dynamic viscosity of the fluid and γ_w is wall shear rate which is proportional to the near-wall velocity gradient. Therefore the closer to the wall that the velocity can be determined, the more accurate τ_w can be calculated. The error associated with this calculation is largely influenced by the technique used to obtain the near-wall velocity measurements within a fluid environment and, specifically, how close to the wall a given technique can resolve the fluid velocity. Techniques including pulsed and spectral Doppler and MRI are generally only able to resolve velocity to approximately 0.9 mm/sec and therefore provide a very poor estimate of WSS (Katritsis et al. 2007). Conversely, if we assume that the geometry of a vascular region can be accurately reproduced, CFD can provide a much better estimate of WSS since the distance from the vascular wall is only limited by the size of the finite element mesh and the computational resources needed to solve the applicable fluids equations for the elements of the mesh. From wall shear stress, a parameter called oscillatory shear index can be calculated and characterizes flow separation from the vascular wall. More specifically, it ranges between 0 and 0.5 where lower OSI values indicate WSS is oriented predominately in the primary direction of blood flow while a value of 0.5 is indicative of bi-directional WSS with a time-averaged value of zero throughout the cardiac cycle. OSI is calculated as

$$OSI = \frac{1}{2}\left(1 - \frac{\tau_{mean}}{\tau_{mag}}\right) \qquad \text{2.10}$$

2.4.4   Quantification and visualization of simulation results

For each outlet in the CFD model BP and flow were quantified from the simulation results and values were scrutinized to ensure they matched the physiologically measured BP (within 5 mmHg) and flow (within 5%) values for each patient or subject. Instantaneous and time-average WSS as well as OSI were calculated for each element on the wall of the mesh. From these files localized measurements were made in specific locations of the model.

Blood flow velocity, BP, WSS and OSI results were visualized using cvSim and an open source software project ParaView (Kitware, Inc., Clifton Park, New York). Previous studies have demonstrated that spatiotemporal alterations in WSS indices may be associated with local cellular alterations (Suo et al. 2007) and it is known that vessels adjust their caliber whenever possible to restore indices of WSS a seemingly preferred level. This concept is known as biomechanical homeostasis and it has been proposed that the homeostatic value is not the same for each vascular region. Consistent with this principle, and to determine cutoff values for quantification of potentially deleterious distributions of TAWSS and OSI, the average value of each quantity was determined from the collection of Normal patients in the vicinity of the descending thoracic aorta. In addition to the entire area of the thoracic aorta subjected to low WSS or elevated OSI, the area of the thoracic aorta distal to the LSA experiencing adverse values of these indices was also quantified.

2.4.5 Mesh Independence

As discussed above, the flow solver used to run simulations utilizes an adaptive meshing technique to generate highly refined anisotropic meshes from subsequent mean and pulsatile simulations for each patient. Studies have demonstrated that it is difficult to obtain WSS results without any error for complex arterial flows without the use of adaptation of meshes (Prakash and Ethier 2001). Requirements for mesh resolution to accurately computationally simulate complex 3D arterial flows in complex geometries have been described (Prakash and Ethier 2001). The mesh was refined adaptively until mesh independence was obtained where the criteria for mesh independence was established as <0.09 dyn/cm^2 between consecutive meshes. Thus, meshes for all cases were adaptively refined until the third or fourth generation anisotropic mesh was obtained or until further mesh adaptation became too computational intensive. The final meshes for the CoA patients and the normal subjects contained approximately 3 million elements and a description of the increase in number of elements with successive meshes is proved in Table 4 below.

Table 4. Mesh statistics for the six Normal subjects and six CoA patients

Normal subjects					Coarctation patients				
Subject number	Number of elements				Patient number	Number of elements			
	Mesh 1	Mesh2	Mesh3	Mesh4		Mesh1	Mesh2	Mesh3	Mesh4
1	627204	609285	1704619	3536360	1	838869	1087189	2551585	3807251
2	659800	763934	1913847	3548348	2	772265	1173316	2153288	3263436
3	471912	698523	1888644	2864469	3	630666	740950	1816022	2437725
4	531871	596846	1608450	3236981	4	756154	842576	2298087	3093804
5	716733	798310	2106098	3268267	5	804381	814928	2128585	3014321
6	514907	622925	1809313	3009854	6	730159	807587	2357241	3093804

2.5 Data Analysis

The anisotropic nature of refined meshes made it non trivial to extract scalar information (TAWSS or OSI data) at regular intervals along the axis or circumference of completed CFD simulations. A number of advanced quantification programs were therefore written by Laura Ellwein, Ph.D. to extract results at predetermined circumferential and axial locations of each CFD model.

A set of locations were chosen along the centerline path of each branch based on a user-defined axial increment for the analysis. At a given location, the equation of a plane orthogonal to the centerline path was calculated and points closest to the plane were queried such that the collection of points were well distributed around the circumference of the vessel (about 120). To determine the circumferential location of a given point, the

analysis points were mapped to a virtual set of points via a set of rotations. The path point

mapped to the origin and the virtual points formed a thin cylindrical contour close to the

xy-plane in the shape of the vessel cross-section with negligible z-component.

Circumferential location (angle) was then calculated by the arctangent of the (x,y)

components of the virtual points and this angle was associated with the original set of

analysis points. Interpolation was used to find (x,y,z) and WSS for points at 0, 90, 180,

and 270 degrees where necessary. The values of the scalar quantity (TAWSS or OSI) for

individual interpolated points were calculated as the weighted average of the scalar

quantity at the four nearest nodes, based on their distance from the point. A 2D moving

average filter weighted filter with 5 horizontal points and 3 vertical points was applied to

the extracted scalar data. The filter had more resolution in the circumferential direction

due to the higher number of points obtained in the circumferential direction. An initial

selection of circumferential resolution was interpolated to 360 equally spaced points

along the circumference. For axial plots, the resolution was selected based on the

diameter of the descending aorta of the individual subject or patient. Axial resolution was

chosen at $1/8^{th}$ of the descending aorta diameter. Axial data was extracted along the

anatomical right, anatomical left, outer and inner curvatures. The distal end of the LSA

served as the starting position for axial plots. By convention and to account for

differences in patient size, quantification locations along the length of the descending

aorta are expressed in terms of outlet diameters. The outlet diameter for each patient is

equal to this dimension at the descending thoracic aorta.

TAWSS data was normalized with respect to the cardiac index (CI) of each

normal subject and CoA patient. While this normalization can mask local fluctuations in

indices of WSS as well as potential homeostatic values for a given patient, the approach

was nonetheless performed to obtain patterns reflective of the collective CoA patient and

Normal subject populations consistent with specific aims of the investigation. CI values

were calculated from a ratio of cardiac output (CO) to body surface area (BSA) where

CO values were obtained from the PCMRI data and BSA was determined using patient

height and weight. OSI values were not normalized as this index is already a normalized

parameter.

The total length of the thoracic aorta centerline paths of the six Normal subjects

and the six Dacron patients were calculated to demonstrate the difference in arch

geometries between the two populations. Tortuosity in the transverse aortic arch for the

six Normal subjects and six Dacron patients was determined by quantifying the radius of

curvature (ROC) as previously described (Mirnajafi et al. 2005). Briefly, the geometry of

the aortic arch was determined by fitting every point on the path to a second order

polynomial give n as,

$$y = ax^2 + bx + c \qquad\qquad 2.11$$

the radius of curvature, r, of the aortic arch at every point in the path was determined by

using the relations

$$ROC = \frac{(1 + (y')^2)^{3/2}}{y''} \qquad\qquad 2.12$$

An average of the ROC values determined at each point was obtained to give the mean radius of curvature in a particular plane. Similarly, ROC in the orthogonal plane was also determined.

The numerical data for all results including TAWSS and OSI is expressed as mean ± Standard error of the mean (SEM). Mean values for BP, blood flow, TAWSS and OSI were compared between investigational groups using Student's 2-sample t-test. Minitab 15® software (Minitab, Inc., State College, PA) was used for all statistical analysis and a P value < 0.05 was considered significant for all comparisons.

Chapter 3 – Results

3.1. Measured and calculated blood flow indices for Normal subjects and Dacron patients

Cardiac output quantified using PCMRI data for Normal subjects and Dacron patients is shown in Table 5. There were no differences in CO between groups (Normal: 6.12±0.5 vs. Dacron: 5.50±0.5 L/min). Cardiac indices quantified from CO and body surface area were within published normal values for Normal subjects (Seear, Webber, and Leblanc 1994) and did not significantly differ from Dacron patients (2.61±0.2 vs. 2.7±0.2 L/min/m^2, respectively, Table 5). Distributions of cardiac output to the head and neck vessels are also provided in Table 6. While there were no differences in blood flow to the innominate artery, there was a significant increase in blood flow to the LCCA in patients treated by Dacron patch as compared to Normal subjects (8.7±0.5% vs. 7.0±0.4%, respectively, P <0.05). Conversely, blood flow distribution to the LSA in Dacron patients was nearly half that observed in Normal subjects (6.0±0.7% vs. 11.6±0.8%, respectively, P <0.05).

Table 5. Measured and calculated blood flow indices for Normal subjects and Dacron patients respectively. Patient 1 = 32 yo male, 2 = 25 yo male, 3 = 33 yo male, 4 = 33 yo female, 5 = 26 yo male and 6 = 26 yo male. * Statistically different from Normal subjects ($P < 0.05$).

	Patient No.	CO (L/min)	CI (L/min/m^2)	IA (% of CO)	LCCA (% of CO)	LSA (% of CO)
NORMAL	1	7.24	2.86	19.3	8.3	14.8
	2	7.91	3.28	18.6	7.4	11.2
	3	5.46	2.43	18.8	7.2	10.8
	4	4.85	2.13	14.1	7.3	12.0
	5	5.55	2.63	22.1	6.3	12.1
	6	5.70	2.32	15.8	5.5	8.5
	Average ± SEM	**6.12±0.5**	**2.61±0.2**	**18.1±1.1**	**7.0±0.4**	**11.6±0.8**
DACRON	1	5.86	2.53	18.0	8.6	7.3
	2	6.68	3.44	16.4	6.5	8.1
	3	5.69	2.65	14.9	8.7	5.7
	4	3.54	2.28	19.2	8.3	6.2
	5	4.91	2.53	21.7	10.3	2.9
	6	6.33	3.18	20.1	9.6	5.78
	Average ± SEM	**5.50±0.5**	**2.77±0.2**	**18.4±1.0**	**8.7±0.5***	**6.0±0.7***

3.2. Blood pressure indices in normal subjects and Dacron patients

Systolic, diastolic, mean and pulse blood pressure values measured immediately following the clinical imaging session for Dacron patients are provided in Table 6 and are not statistically different from those ascertained from the literature (Drizd, Dannenberg, and Engel 1986) for Normal subjects using their anatomic characteristics.

Table 6. Blood pressure values for Normal subjects and Dacron patients. Patient 1 = 32 yo male, 2 = 25 yo male, 3 = 33 yo male, 4 = 33 yo female, 5 = 26 yo male and 6 = 26 yo male.

	Patient No.	Systolic Blood Pressure (mmHg)	Diastolic Blood Pressure (mmHg)	Mean Blood Pressure (mmHg)	Pulse Pressure (mmHg)
NORMAL	1	125	79	97	46
	2	124	76	97	48
	3	125	73	87	39
	4	112	79	95	46
	5	125	79	97	46
	6	125	79	96	46
	Average ± SEM	**123±2**	**78±1**	**95±2**	**45±1**
DACRON	1	137	64	95	74
	2	114	80	91	34
	3	107	64	81	43
	4	110	65	85	46
	5	117.5	72	81	46
	6	145	89	111	56
	Average ± SEM	**122±6**	**72±4**	**91±5**	**50±6**

3.3. Indices of aortic morphology

Tortuosity in the transverse arch of Normal subjects and Dacron patients was determined by quantifying the ROC in two orthogonal planes as previously described (Mirnajafi et al. 2005) and discussed above. Results are provided in Table 7. While the radius of curvature in Normal subjects was generally greater in both the lateral and top view planes as compared to the Dacron patients, this difference did not reach significance when comparing the collective groups of patients. It is important to note that Dacron patients 1, 4 and 5 include pronounced out-of-plane thoracic aorta curvature upon visual inspection that was not delineated as statistically significant using the approach of Mirnajafi et al.

However, the total length of the thoracic aorta centerline path discussed in the Methods section is also reflective of differences in arch geometries between Normal subjects and Dacron patients. These lengths are provided in Table 8 and demonstrate that Dacron patients collectively have a significantly longer thoracic aorta than Normal subjects (295 ± 8 mm vs. 263 ± 4 mm, respectively, $P < 0.05$).

Table 7. Radius of curvature measured in the coarctation patients treated with Dacron patch aortoplasty and the six corresponding age and gender matched Normal subjects. Patient 1 = 32 yo male, 2 = 25 yo male, 3 = 33 yo male, 4 = 33 yo female, 5 = 26 yo male and 6 = 26 yo male.

	NORMAL		DACRON	
Patient No.	**ROC in lateral view (mm)**	**ROC in top view (mm)**	**ROC in lateral view (mm)**	**ROC in top view (mm)**
1	69	65	75	65
2	67	71	75	36
3	56	109	80	62
4	83	56	47	82
5	74	72	69	83
6	71	75	65	72
Average ± SEM	**70±4**	**75±7**	**69±5**	**67±7**

Table 8. Total length of the thoracic aorta values measured in the six coarctation patients treated with Dacron patch aortoplasty and the six corresponding age and gender matched normal subjects. Patient 1 = 32 yo male, 2 = 25 yo male, 3 = 33 yo male, 4 = 33 yo female, 5 = 26 yo male and 6 = 26 yo male. * Statistically different from Normal subjects (P < 0.05).

Patient No	Total length of Thoracic aorta in Normal subjects (mm)	Total length of Thoracic aorta in Dacron patients (mm)
1	273	314
2	266	292
3	250	260
4	273	288
5	266	309
6	249	306
Average ± SEM	**264±4**	**295±8***

3.4. CFD simulation results

3.4.1 Temporal Blood Flow Velocity

Temporal distributions of blood flow velocity in Normal subjects and Dacron patients are provided in Figures 11, 12 and 13 as streamlines during early systole, mid-to-late systole, and end systole consistent with time points selected by Kilner et al. in their description of blood flow patterns in the thoracic aorta (Kilner et al. 1993). For the Normal subjects, velocity is fully attached with a magnitude of 40 to 80 cm/s and streamlines are skewed towards the inner wall during early systole (Figure 11, row 1). Importantly, there is continuous, seemingly laminar flow from the aorta to the head and neck vessels for each of the six patients. While overall skewing of velocity towards the inner wall of curvature is also observed for Dacron patients, they also display much less consistent patterns of velocity including magnitudes < 20 cm/s and swirling in patients 1, 2, 4 and 5 or elevated velocity > 100 cm/s in locations of residual narrowing including the coarctation region of patient 3 and the transverse arch of patient 6 (Figure 11, row 2). These patterns lead to localized flow disruptions in several Dacron patients as blood flows from the arch to the arteries of the head and neck, and particularly the LSA, during early systole. During mid-to-late systole velocity streamlines obtained from CFD simulation results show skewing of velocity along the outer curvature and the development of right-handed helical flow in the aortic arch of Normal subjects consistent with prior reports (Kilner et al. 1993; Wentzel et al. 2005). This time during the cardiac cycle is also associated with elevated (> 100 cm/s), forward-directed velocity in the

absence of swirling or vortices in the descending thoracic aorta of these subjects (Figure

2, row 1). While skewing of velocity toward the outer wall and the development of

helical flow also occurs in Dacron patients 1-3, these patterns are not ubiquitously

observed in simulation results of all patients at mid-to-late systole and streamlines during

this time are more erratic in the descending thoracic aorta (Figure 12, row 2). Velocity

streamlines at end systole primarily show swirling and rotational flow throughout the

aorta of both investigational groups along with convective acceleration in areas of

residual narrowing for Dacron patients (Figure 13, rows 1 and 2).
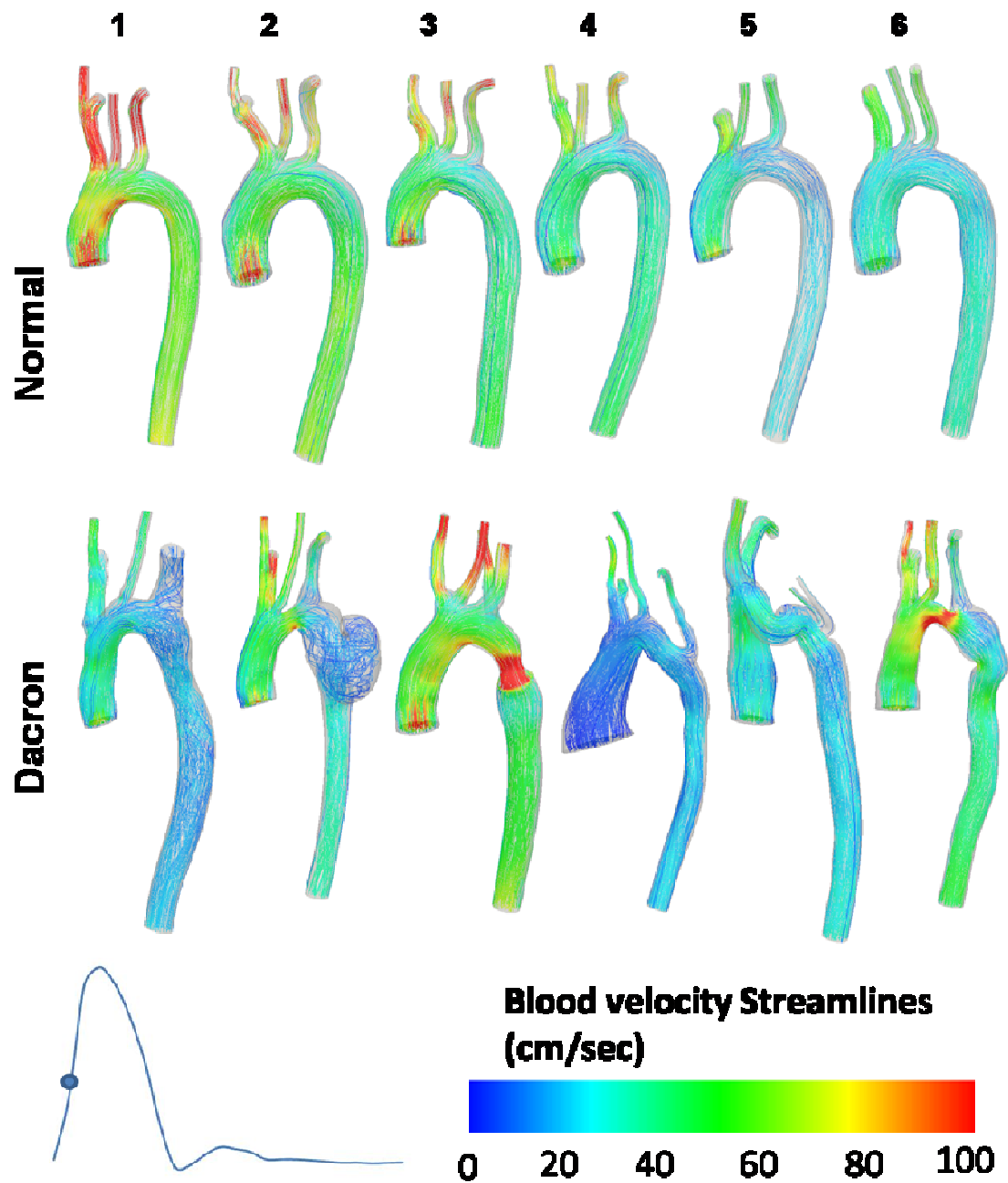
Figure 11. Variations in blood flow velocity streamlines at early-systole in the six Normal subjects (top row) and six age and gender matched Coarctation patients with Dacron patch aortoplasty repair (bottom row). Patient 1 = 32 yo male, 2 = 25 yo male, 3 = 33 yo male, 4 = 33 yo female, 5 = 26 yo male and 6 = 26 yo male.
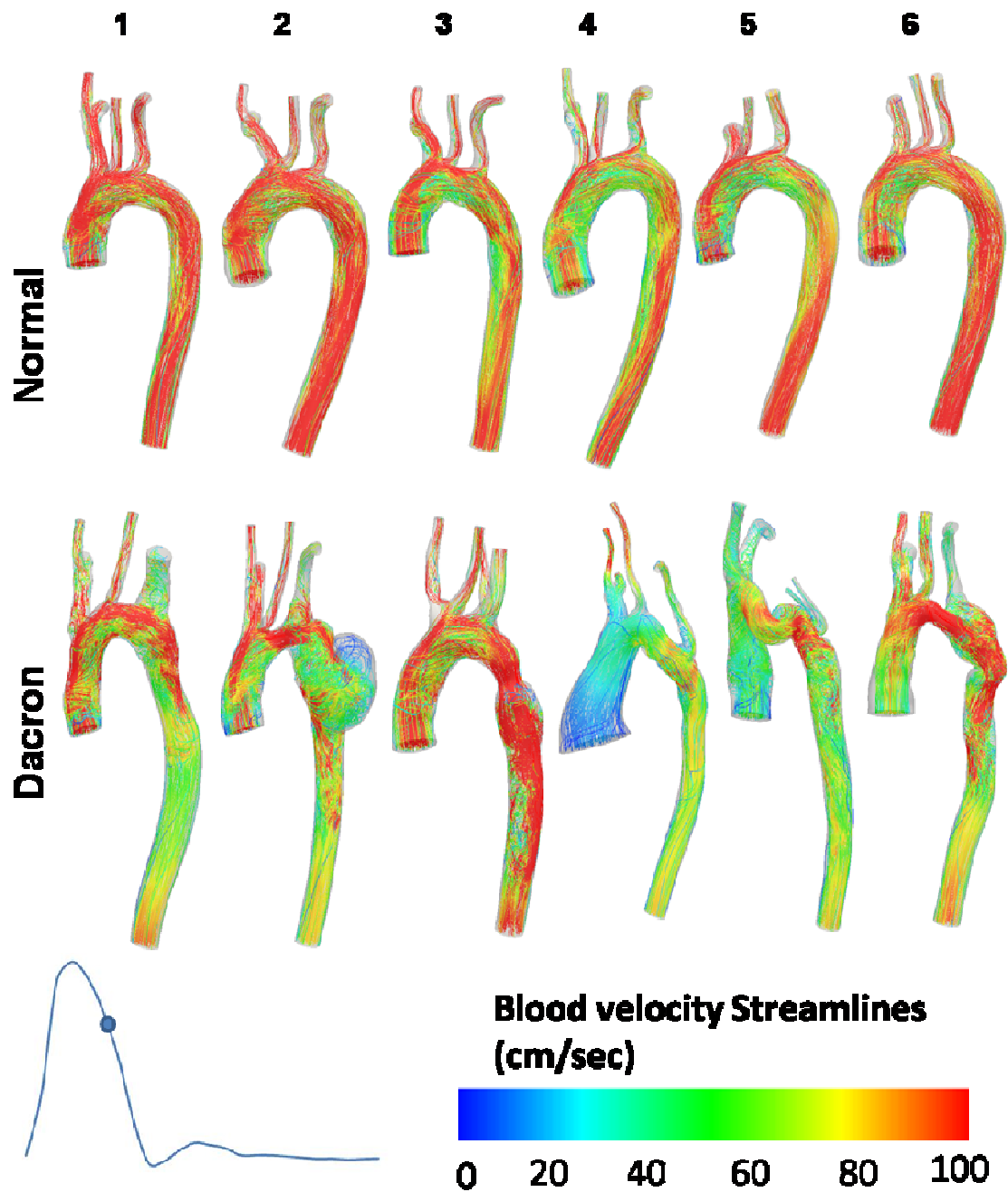
Figure 12. Variations in blood flow velocity streamlines at mid-to-late systole in the six Normal subjects (top row) and six age and gender matched Coarctation patients with Dacron patch aortoplasty repair (bottom row). Patient 1 = 32 yo male, 2 = 25 yo male, 3 = 33 yo male, 4 = 33 yo female, 5 = 26 yo male and 6 = 26 yo male.
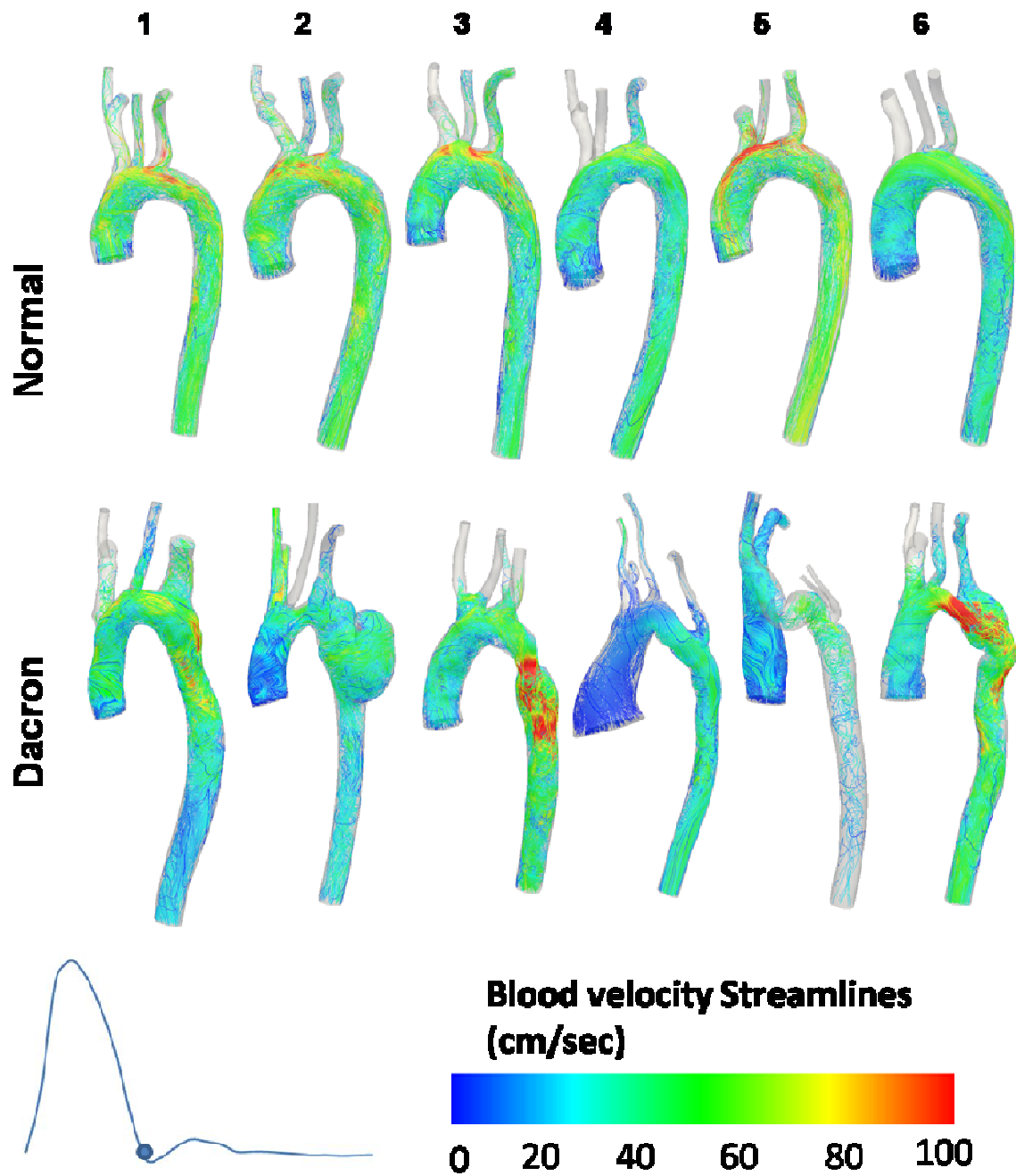
Figure 13. Variations in blood flow velocity streamlines at end systole in the six Normal subjects (top row) and six age and gender matched Coarctation patients with Dacron patch aortoplasty repair (bottom row). Patient 1 = 32 yo male, 2 = 25 yo male, 3 = 33 yo male, 4 = 33 yo female, 5 = 26 yo male and 6 = 26 yo male.

3.4.2. Velocity profiles in the descending thoracic aorta

To further understand and quantify local disparity in blood flow patterns between Normal subjects and Dacron patients, and compare with distributions of WSS presented below, velocity profiles from simulation results were also quantified at select locations in the descending thoracic aorta (Figures 14-17). The top and bottom of velocity profile images represent lumen surfaces along the outer and inner radii of curvature, respectively, and left and right are consistent with their anatomic locations. Using this convention, forward-directed flow would be coming out of the page towards the reader.

Consistent with streamlines presented above, elevated velocity is seen along the inner wall in the vicinity of the transverse arch during early systole for both investigational groups (Figure 14). At mid-to-late systole, counter-rotating vortices begin to form within the center of the transverse arch in Normal patients. This pattern is less consistent for CoA patients treated by Dacron patch which includes two instances of convective flow acceleration through narrowed hypoplastic regions (patients 2 and 6). These respective patterns persist for both groups, but to a lesser extent, during late systole.

Just distal to the LSA (Figure 15) lowest velocity is localized to the outer wall (i.e. top) of curvature for all Normal and Dacron patients during early systole with the exception of Dacron patient 3 where residual narrowing causes elevated velocity. During mid-to-late systole at this location, counter rotating vortices begin to form and are slightly skewed toward the anatomic left portion of the vessel in Normal patients. At 1-2

diameters from the LSA (Figures 16 and 17, respectively) the orientation of these counter-rotating vortices observed in Normal patients becomes progressively more oriented toward the anatomic left position. These trends at respective diameter locations from the LSA in Normal patients continued, but were more modest during end systole. An analogous trend was not ubiquitously observed for CoA patients at each time point due to residual narrowing, out-of-plane motion and the presence of modest or pronounced aneurysms in various patients.
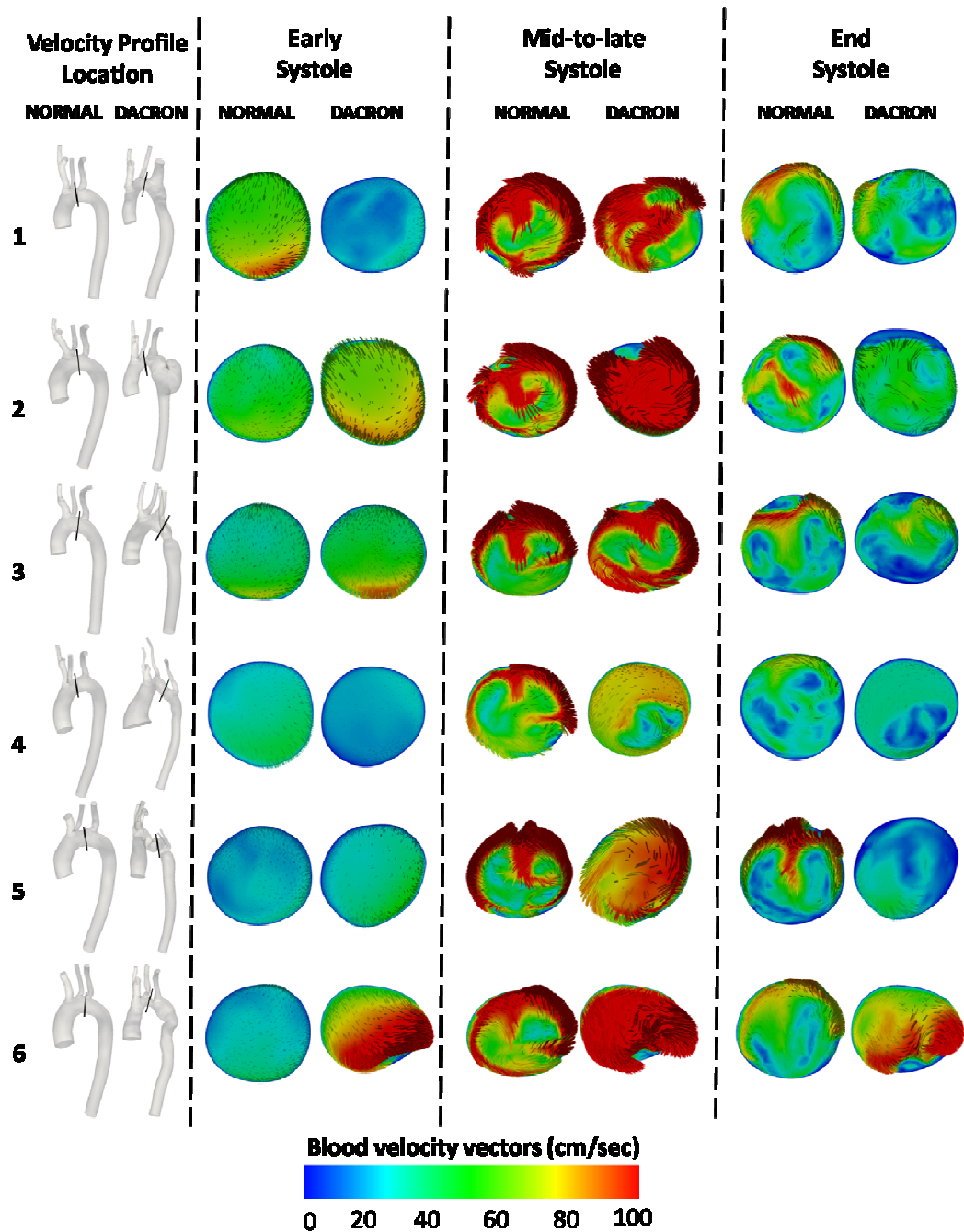
Figure 14. Velocity profiles obtained for cross-sections orthogonal to the transverse arch during early systole (left), mid-to-late systole (middle) and end systole (right) in the six Normal subjects and age and gender matched CoA patients treated with Dacron patch aortoplasty repair. Patient 1 = 32 yo male, 2 = 25 yo male, 3 = 33 yo male, 4 = 33 yo female, 5 = 26 yo male and 6 = 26 yo male.
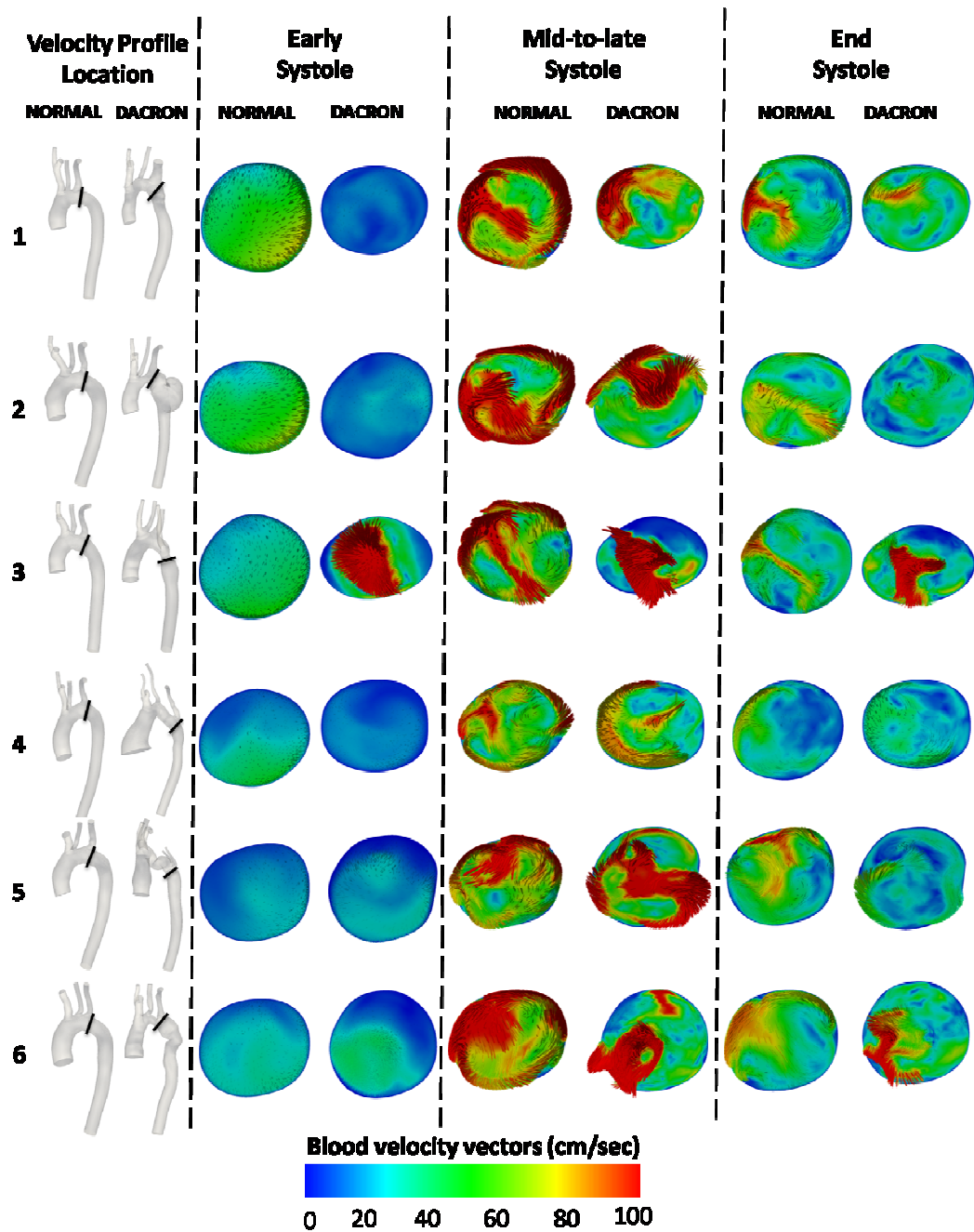
**Figure 15. Velocity profiles obtained for orthogonal cross-sections obtained just distal to the LSA during early systole (left), mid-to-late systole (middle) and end systole (right) in the six Normal subjects and age and gender matched CoA patients treated with Dacron patch aortoplasty repair. Patient 1 = 32 yo male, 2 = 25 yo male, 3 = 33 yo male, 4 = 33 yo female, 5 = 26 yo male and 6 = 26 yo male.**
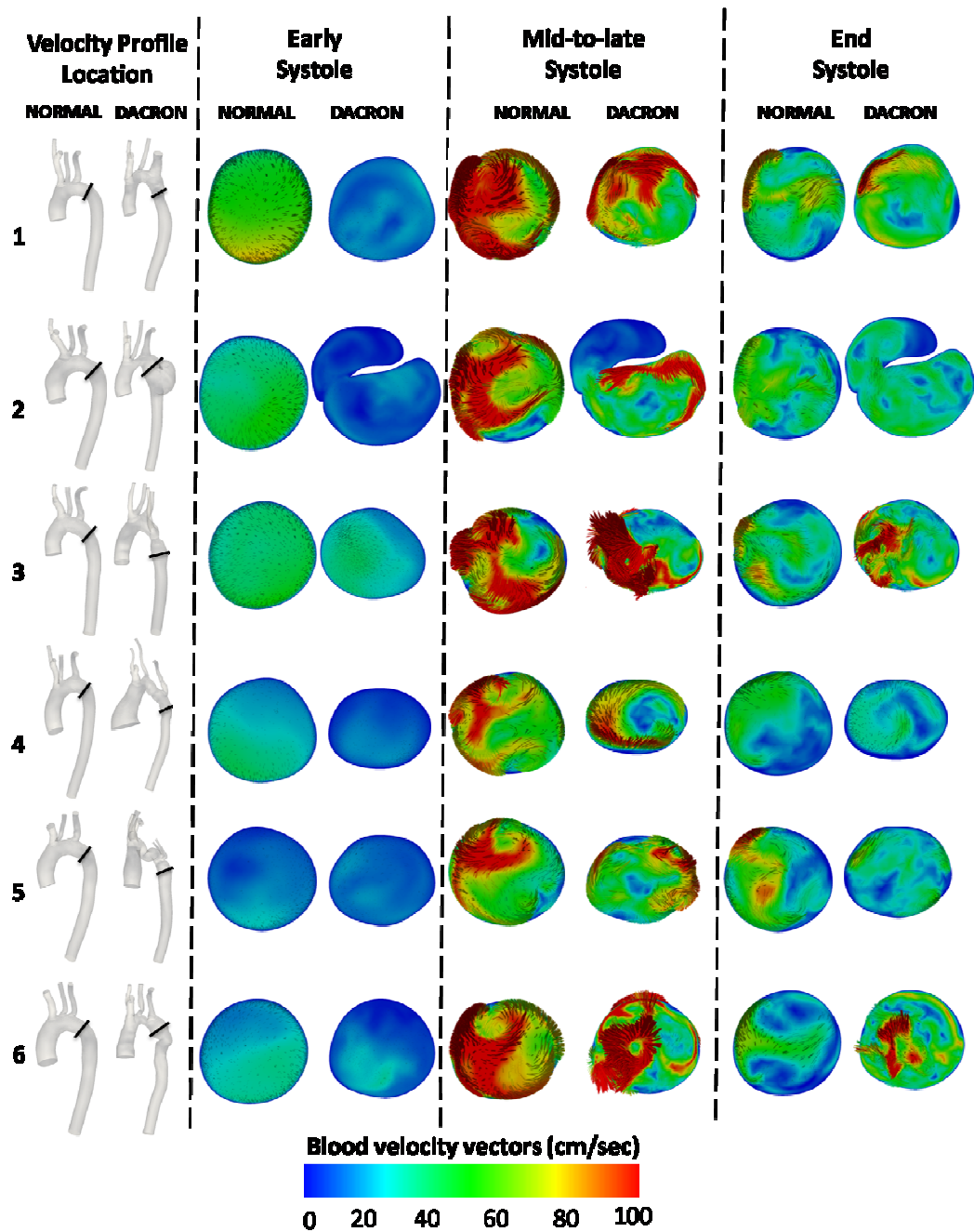
Figure 16. Velocity profiles obtained for orthogonal cross-sections obtained 1 descending aortic diameter distal to the LSA during early systole (left), mid-to-late systole (middle) and end systole (right) in the six Normal subjects and age and gender matched CoA patients treated with Dacron patch aortoplasty repair. Patient 1 = 32 yo male, 2 = 25 yo male, 3 = 33 yo male, 4 = 33 yo female, 5 = 26 yo male and 6 = 26 yo male.
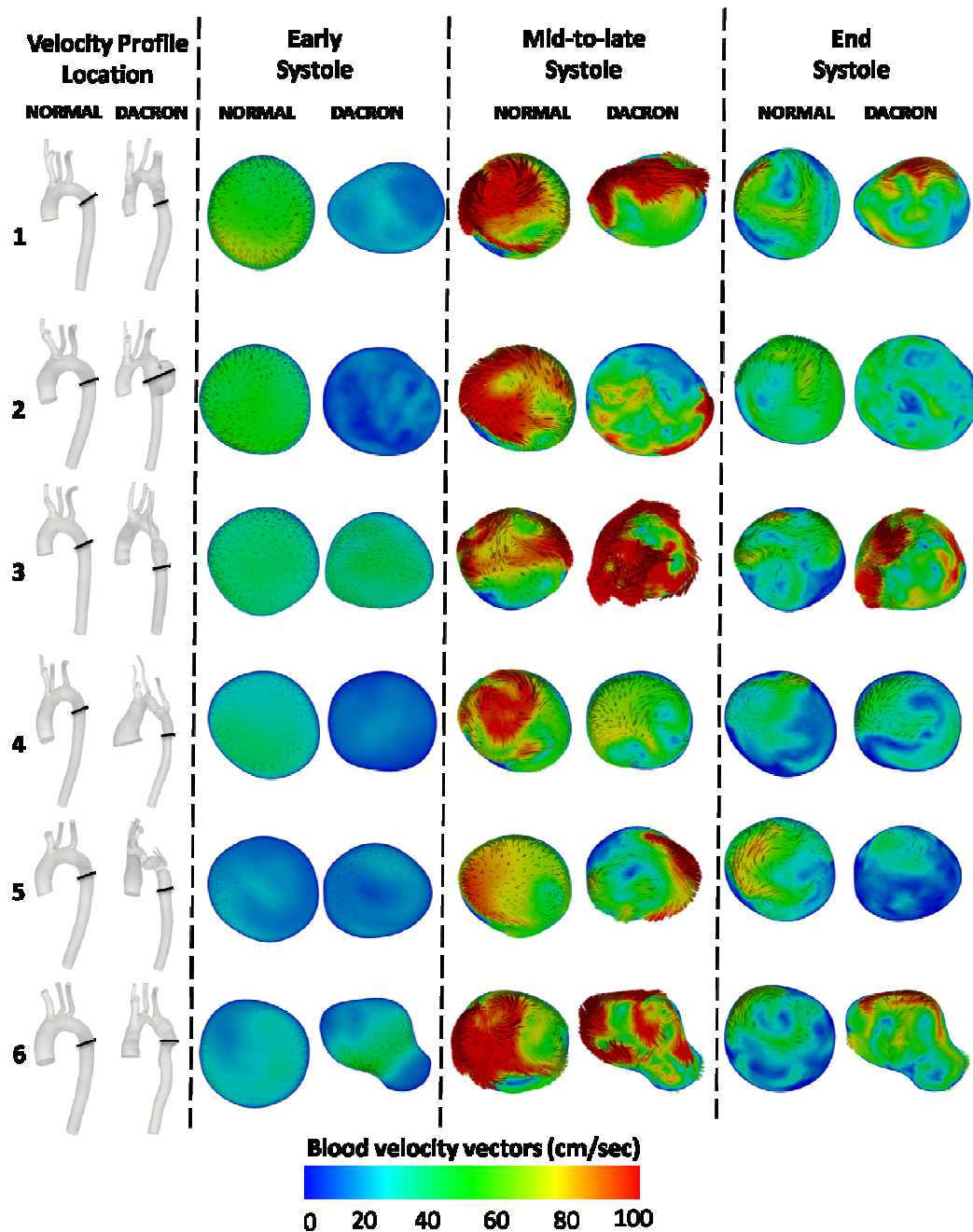
Figure 17. Velocity profiles obtained for orthogonal cross-sections obtained 2 descending aortic diameter distal to the LSA during early systole (left), mid-to-late systole (middle) and end systole (right) in the six Normal subjects and age and gender matched CoA patients treated with Dacron patch aortoplasty repair. Patient 1 = 32 yo male, 2 = 25 yo male, 3 = 33 yo male, 4 = 33 yo female, 5 = 26 yo male and 6 = 26 yo male.

3.4.3. Distributions of WSS in Normal subjects and Dacron patients

Figures 18, 19 and 20 show the variation in spatial distributions of WSS in Normal subjects and Dacron patients at early systole, mid-to-late systole, and end systole, respectively. WSS patterns at each of the three times in the cardiac cycle depicted are generally reflective of the local alterations in blood flow velocity described above and from which they are determined. Previous studies suggest spatiotemporal values of WSS may be associated with local cellular alterations (Suo et al. 2007). The putative, and more common, way of analyzing WSS results utilizes time-averaged WSS values and OSI calculated as described in the Methods section. Thus, images of time-averaged WSS and OSI are presented in Figures 21 and 22, respectively. Previous studies have demonstrated that vessels adjust their caliber whenever possible to restore indices of WSS to a seemingly preferred level, so cutoff values for quantification of potentially deleterious distributions of TAWSS and OSI were determined as the average value of each quantity determined from the collection of Normal patients in the vicinity of the descending thoracic aorta. The values of 13 dynes/cm^2 and 0.14 for TAWSS and OSI, respectively, were therefore used for the quantification below.

In general, elevated TAWSS (> 50 dynes/cm^2) was observed just distal to the ostium of the head and neck vessels and lower TAWSS (< 13 dynes/cm^2) was localized to the inner luminal surface of the descending thoracic aorta in Normal patients. In contrast, TAWSS was not uniformly observed in the ostium of the head and neck vessels of Dacron patients and TAWSS was particularly low in the LSA of 5 out of 6 patients. Regions of elevated TAWSS were, however, observed in locations of residual coarctation

narrowing, transverse arch hyperplasia and out-of-plan curvature. The total area of vessels exposed to low TAWSS was 57±12% for Dacron patients as compared to 45±7% for Normal subjects (Table 9). When only considering the area distal to the LSA, the area of the lumen surface exposed to low TAWSS was 48±8% for Dacron patients as compared to 39±4% for Normal subjects (Table 10).

Normal subjects also had less of the luminal surface exposed to potentially deleterious OSI as compared to Dacron patients (52±12% vs. 41±6%, respectively, and 49±6% vs. 42±5% for the area distal to the LSA), but this difference did not reach significance. Areas of OSI > 0.14, and hence reflective of secondary flow, were confined to the inner lumen surface of the descending thoracic aorta for Normal subjects, particularly near the region of the ductus arteriosus where right-handed helical flow is known to transition into left-handed but more axially-directed flow (Kilner et al. 1993). Regions of OSI > 0.14 for Dacron patients were localized to areas of altered vascular geometry presenting since surgical correction including aneurismal regions (patients 2 and 6) as well as distal to residual narrowings and out-of-plane curvature. Regions of secondary flow were also generally more concentric in the descending thoracic aorta of Dacron patients as compared to Normal subjects. Spatial trends in these indices of TAWSS and OSI are reported below.
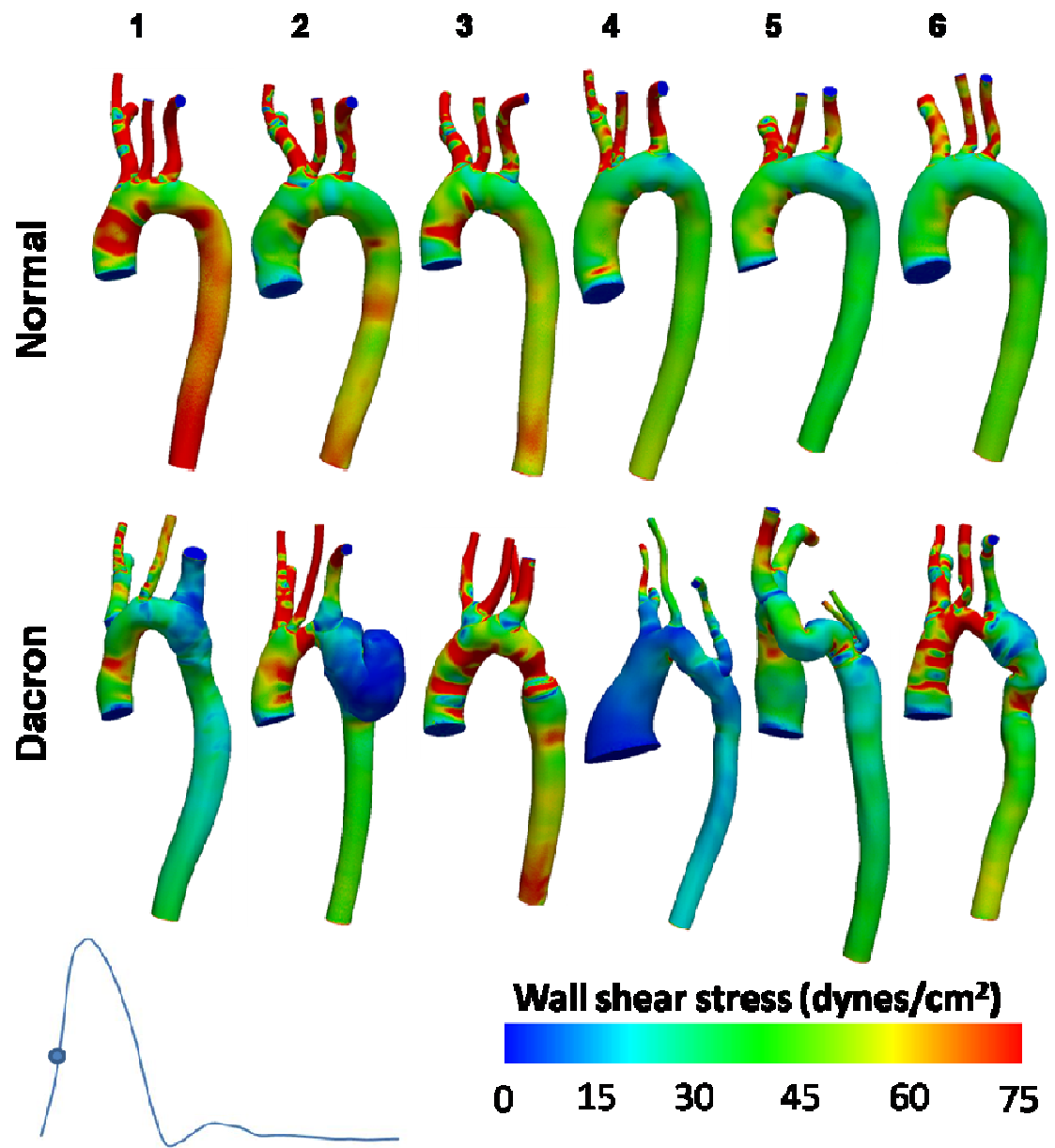
Figure 18. Spatial WSS distributions at early systole in the six Normal subjects (above) as well as age and gender matched patients previously treated for Coarctation by Dacron patch aortoplasty (below). Patient 1 = 32 yo male, 2 = 25 yo male, 3 = 33 yo male, 4 = 33 yo female, 5 = 26 yo male and 6 = 26 yo male.

**Figure 19. Spatial WSS distributions during mid-to-late systole in the six Normal subjects (above) as well as age and gender matched patients previously treated for Coarctation by Dacron patch aortoplasty (below). Patient 1 = 32 yo male, 2 = 25 yo male, 3 = 33 yo male, 4 = 33 yo female, 5 = 26 yo male and 6 = 26 yo male.**
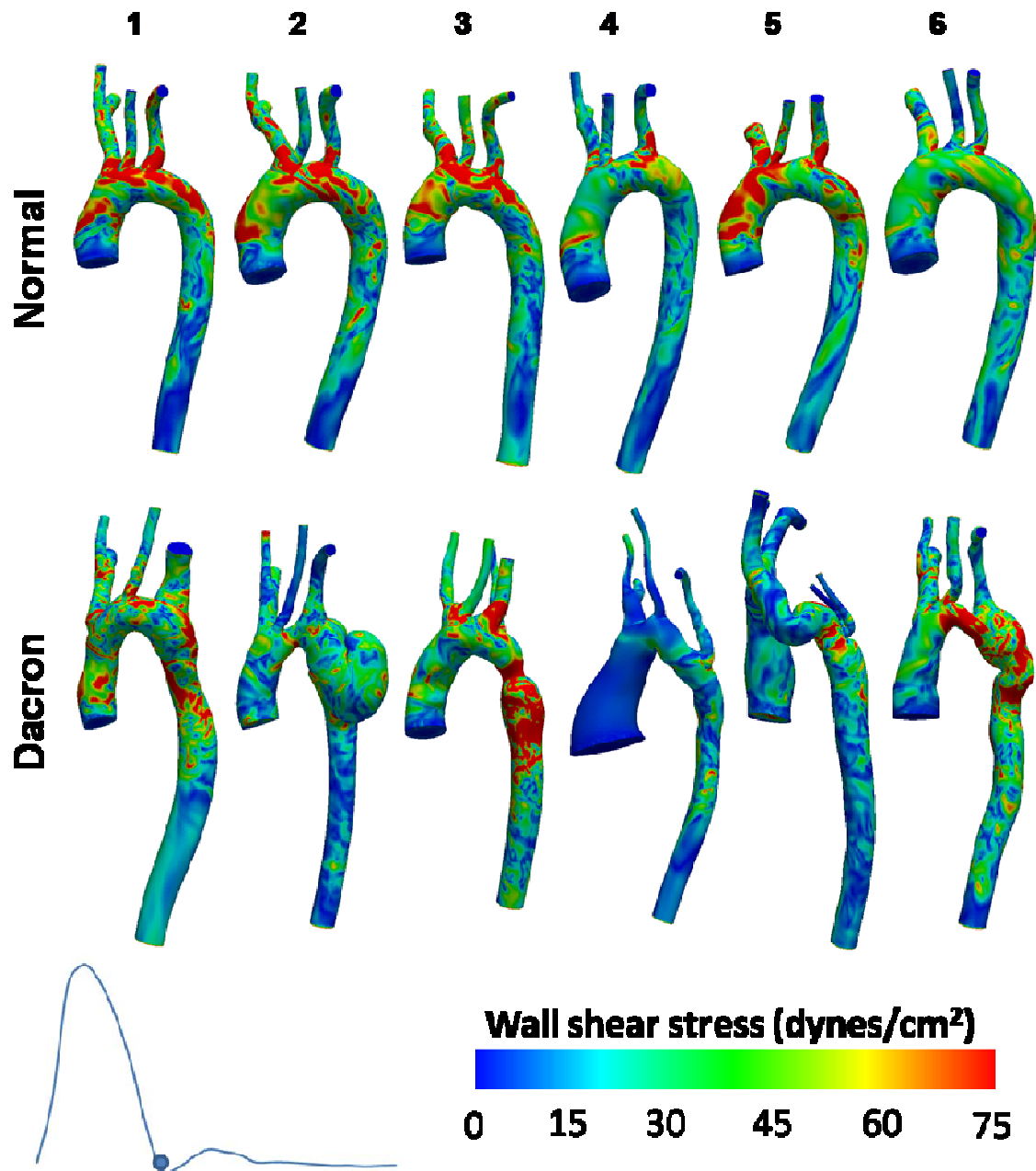
Figure 20. Spatial WSS distributions at end-systole in the six Normal subjects (above) as well as age and gender matched patients previously treated for Coarctation by Dacron patch aortoplasty (below). Patient 1 = 32 yo male, 2 = 25 yo male, 3 = 33 yo male, 4 = 33 yo female, 5 = 26 yo male and 6 = 26 yo male.
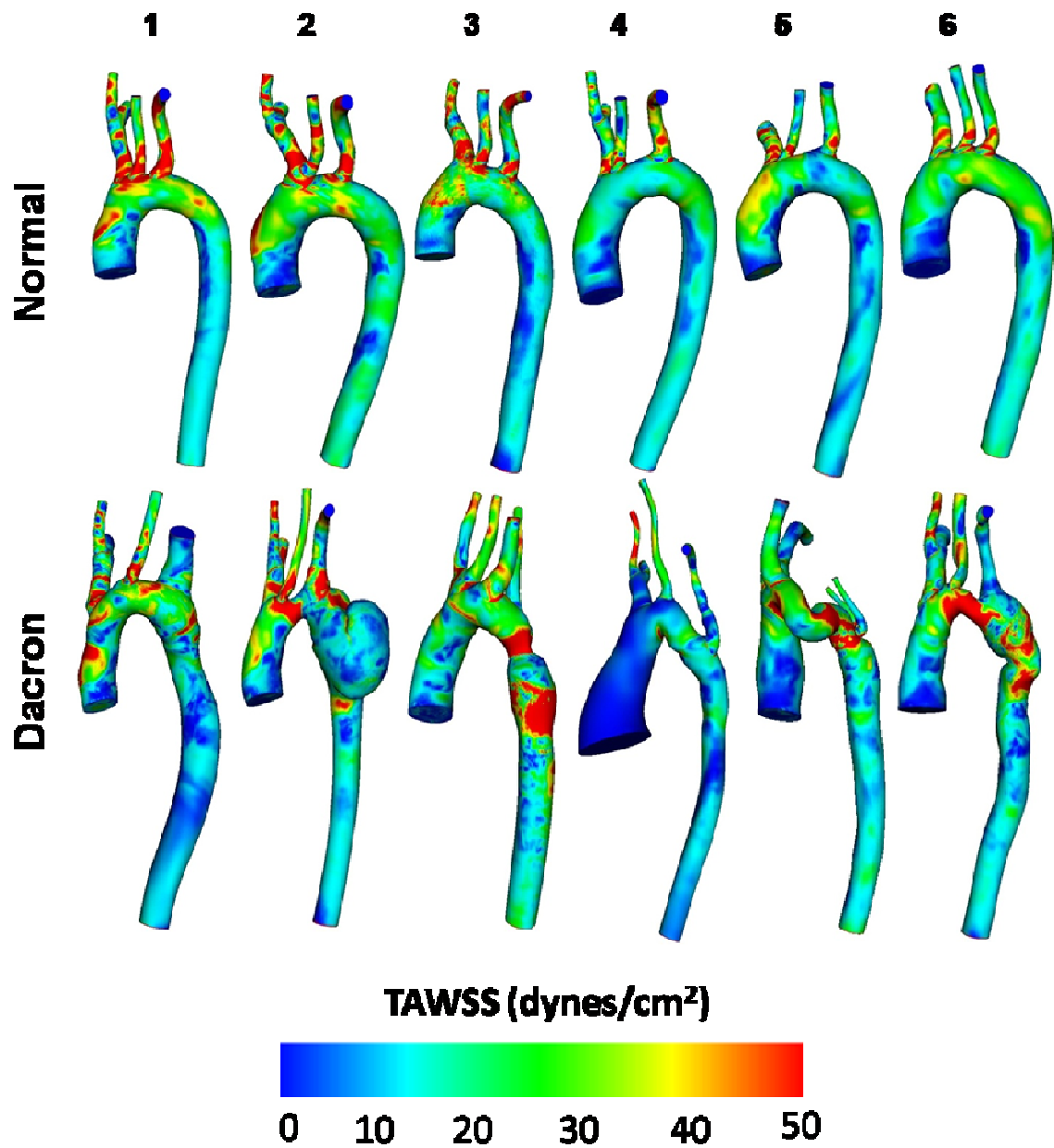
Figure 21. Time-averaged WSS distributions in the six Normal subjects (above) as well as age and gender matched patients previously treated for Coarctation by Dacron patch aortoplasty (below). Patient 1 = 32 yo male, 2 = 25 yo male, 3 = 33 yo male, 4 = 33 yo female, 5 = 26 yo male and 6 = 26 yo male.
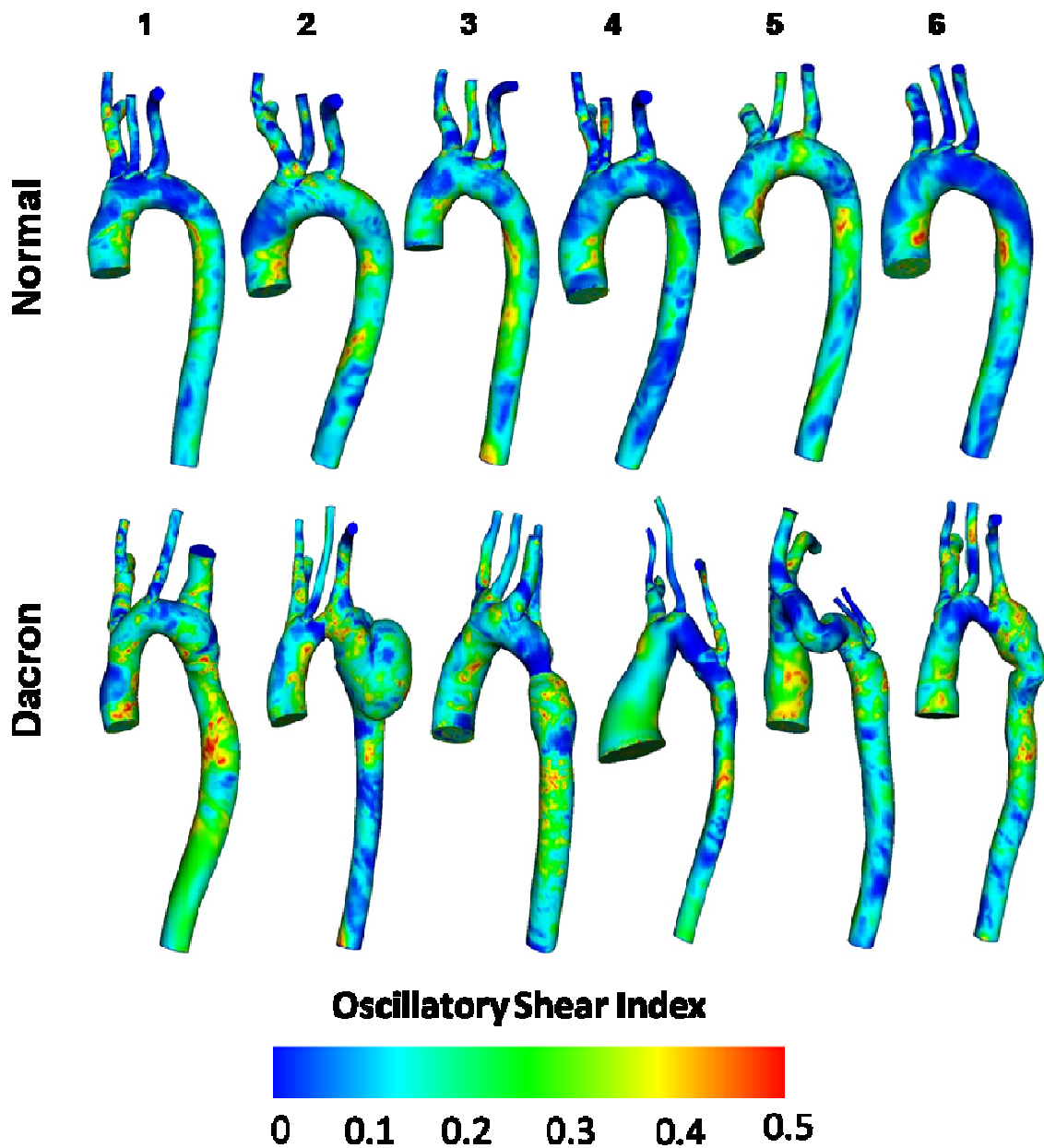
Figure 22. Oscillatory Shear Index for the six Normal subjects (above) as well as age and gender matched patients previously treated for Coarctation by Dacron patch aortoplasty (below). Patient 1 = 32 yo male, 2 = 25 yo male, 3 = 33 yo male, 4 = 33 yo female, 5 = 26 yo male and 6 = 26 yo male.

Table 9. Percentage of the thoracic aorta exposed to TAWSS < 13 dynes/cm^2 and OSI > 0.14 for the six Normal subjects and age and gender matched CoA patients treated with Dacron patch aortoplasty repair, Patient 1 = 32 yo male, 2 = 25 yo male, 3 = 33 yo male, 4 = 33 yo female, 5 = 26 yo male and 6 = 26 yo male. * Statistically different from Normal subjects (P < 0.05).

	NORMAL			DACRON		
Patient No	Total area of the aorta (mm^2)	% of area with TAWSS < 13 dyn/cm^2	% of area with OSI > 0.14	Total area of the aorta (mm^2)	% of area with TAWSS < 13 dyn/cm^2	% of area with OSI > 0.14
1	24543	43	54	30675	55	68
2	24650	24	41	31839	46	41
3	22229	49	52	24586	23	45
4	21613	39	27	26851	78	44
5	21709	47	45	25047	36	39
6	20096	32	34	30223	48	52
Average ± SEM	22473 ± 732	39 ± 4	42 ± 5	*28204 ± 1269	48 ± 8	49 ± 6

Table 10. Percentage of the descending thoracic aorta distal to the LSA exposed to TAWSS < 13 dynes/cm^2 and and OSI > 0.14 for the six Normal subjects and age and gender matched CoA patients treated with Dacron patch aortoplasty repair, Patient 1 = 32 yo male, 2 = 25 yo male, 3 = 33 yo male, 4 = 33 yo female, 5 = 26 yo male and 6 = 26 yo male. * Statistically different from Normal subjects (P < 0.05)
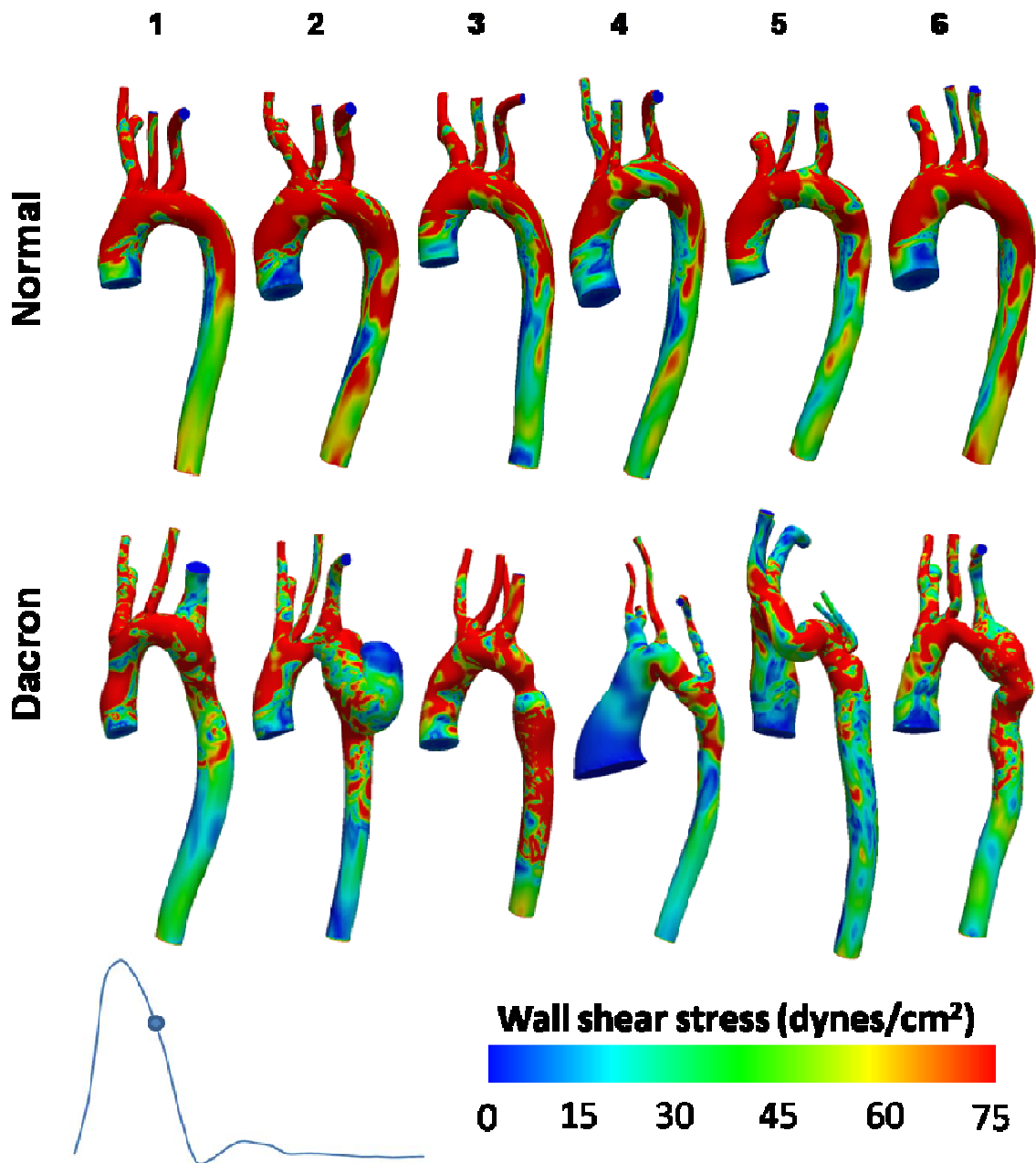
	NORMAL			DACRON		
Patient No	Area of the aorta distal to LSA (mm^2)	% of area with TAWSS < 13 dyn/cm^2	% of area with OSI > 0.14	Area of the aorta distal to LSA (mm^2)	% of area with TAWSS < 13 dyn/cm^2	% of area with OSI > 0.14
1	12444	41	36	15757	78	85
2	12091	27	46	19245	59	37
3	11693	68	63	9763	22	56
4	10821	41	21	8895	85	39
5	11563	60	44	9362	42	36
6	10391	33	35	15002	49	53
Average ± SEM	11500 ± 315	45 ± 7	41 ± 6	13004 ± 1743	57 ± 12	52 ± 12

3.4.4. Local quantification of TAWSS and OSI indices

Figure 23 shows a schematic representation of the four axes along which TAWSS and OSI data were quantified by extracting the values from simulation results. To account for differences in patient size and corresponding cardiac function, TAWSS were normalized by dividing by each patient's cardiac output.

Blue - 0 degree (Outer right curvature)
Purple – 90 degree (Outer top curvature)
Green – 180 degree (Outer left curvature)
Red – 270 (Inner bottom curvature)
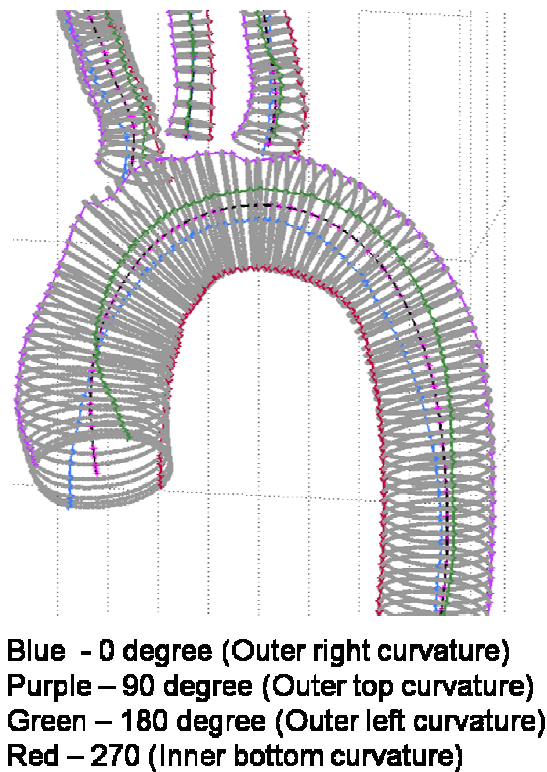
Figure 23. Anatomic locations of the four axes along which axial TAWSS and OSI plots were quantified.

Figures 24 and 25 depict TAWSS distal to the LSA and ensemble-averaged for Normal subjects and Dacron patients along the four axes shown above. Distributions of TAWSS along the left and right walls of the thoracic aorta in Normal patients are similar

with the exception of the region two diameters distal to the LSA where there is reduced TAWSS along the left luminal surface. Interestingly, Dacron patients did not display this spatial heterogeneity in TAWSS between the second and third diameter from the LSA (P <0.05). In Normal patients TAWSS is higher along the outer luminal surface, as compared to the inner luminal surface, immediately distal to the LSA, but then drops below that along the inner surface until approximately 0.75 diameters distal to the LSA. An area of lower normalized TAWSS was also observed two diameters distal to the LSA along the inner and outer luminal surfaces of Normal subjects, but not Dacron patients (P <0.05).

Figures 26 and 27 similarly depict ensemble-averaged axial OSI plots for the thoracic aorta distal to LSA. As seen in Figure 26, OSI increases significantly along the outer curvature between the third and fourth diameters and just distal to the LSA for Dacron patients. OSI was also higher in Dacron patients as compared to Normal subjects between the third and fourth diameter and the fourth and fifth diameter along the anatomic right and the left curvatures, respectively.
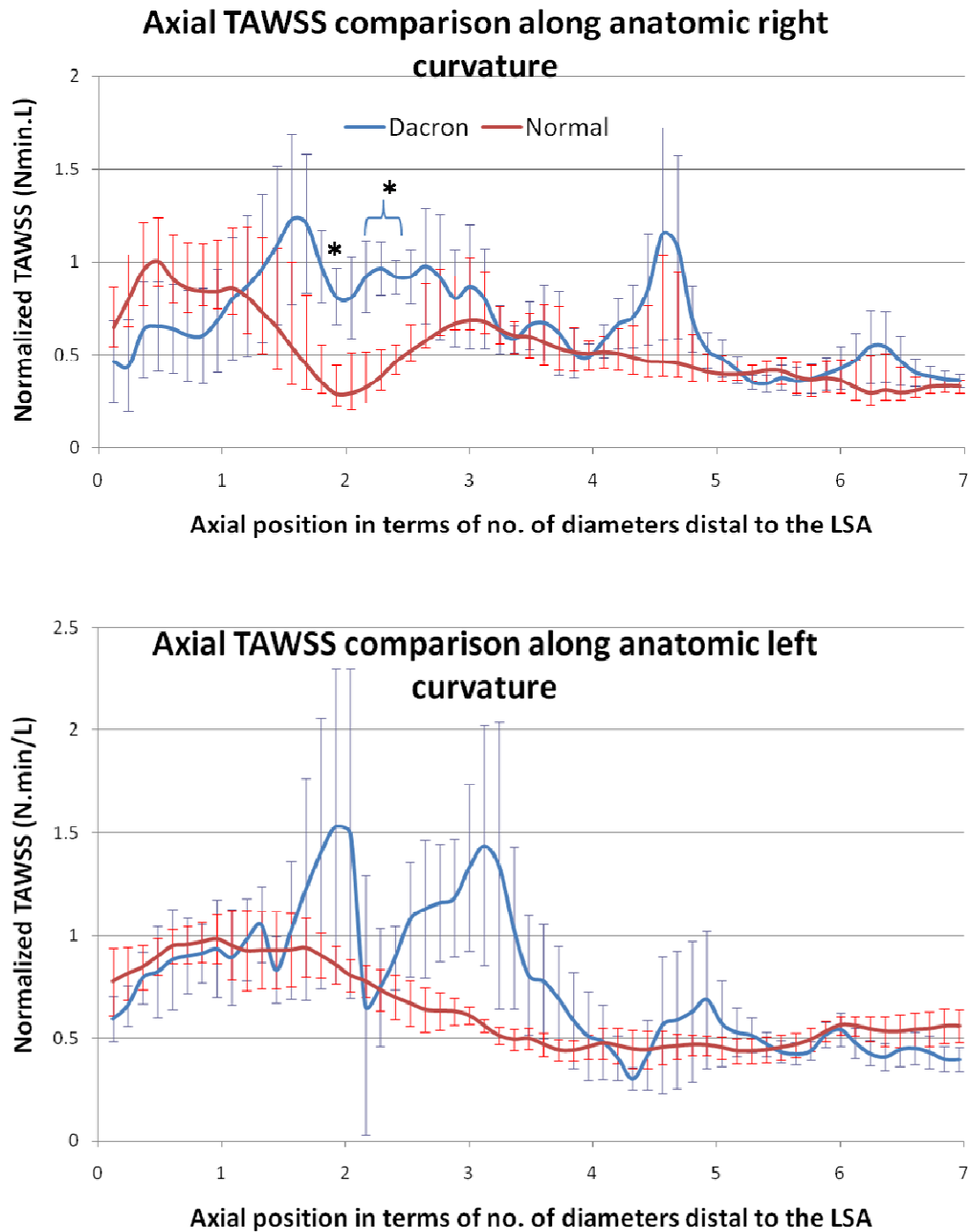
Figure 24. Ensemble-averaged axial TAWSS plots comparing Dacron patients with normal subjects along anatomic right (top) and anatomic left (below) curvature. * Statistically different from Normal subjects (P < 0.05). Data are expressed as mean ± SEM.
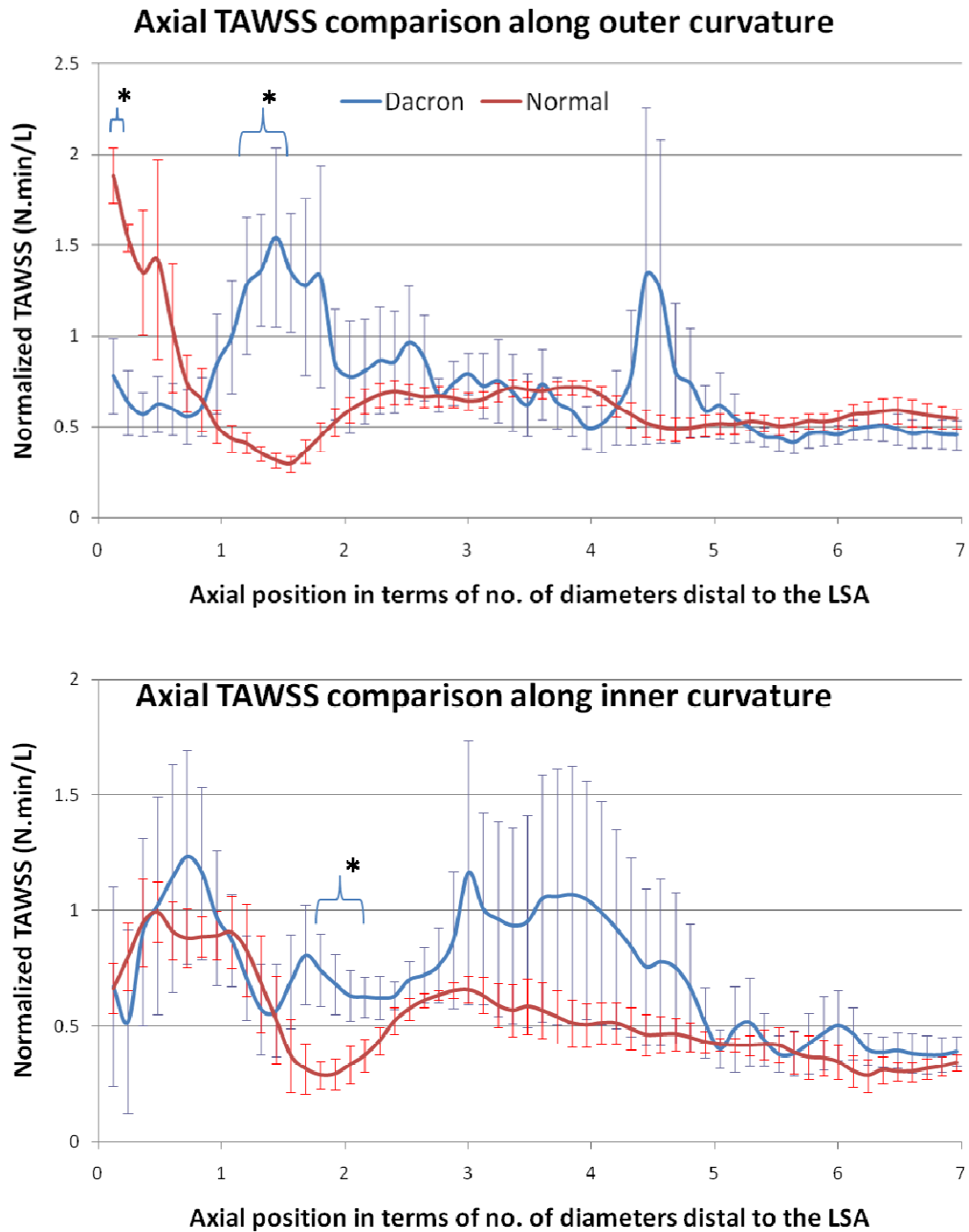
Figure 25. Ensemble-averaged axial TAWSS plots comparing Dacron patients with normal subjects along outer (top) and inner (below) curvature. * Statistically different from Normal subjects (P < 0.05). Data are expressed as mean ± SEM.

Axial OSI comparison along outer curvature

Axial OSI comparison along inner curvature
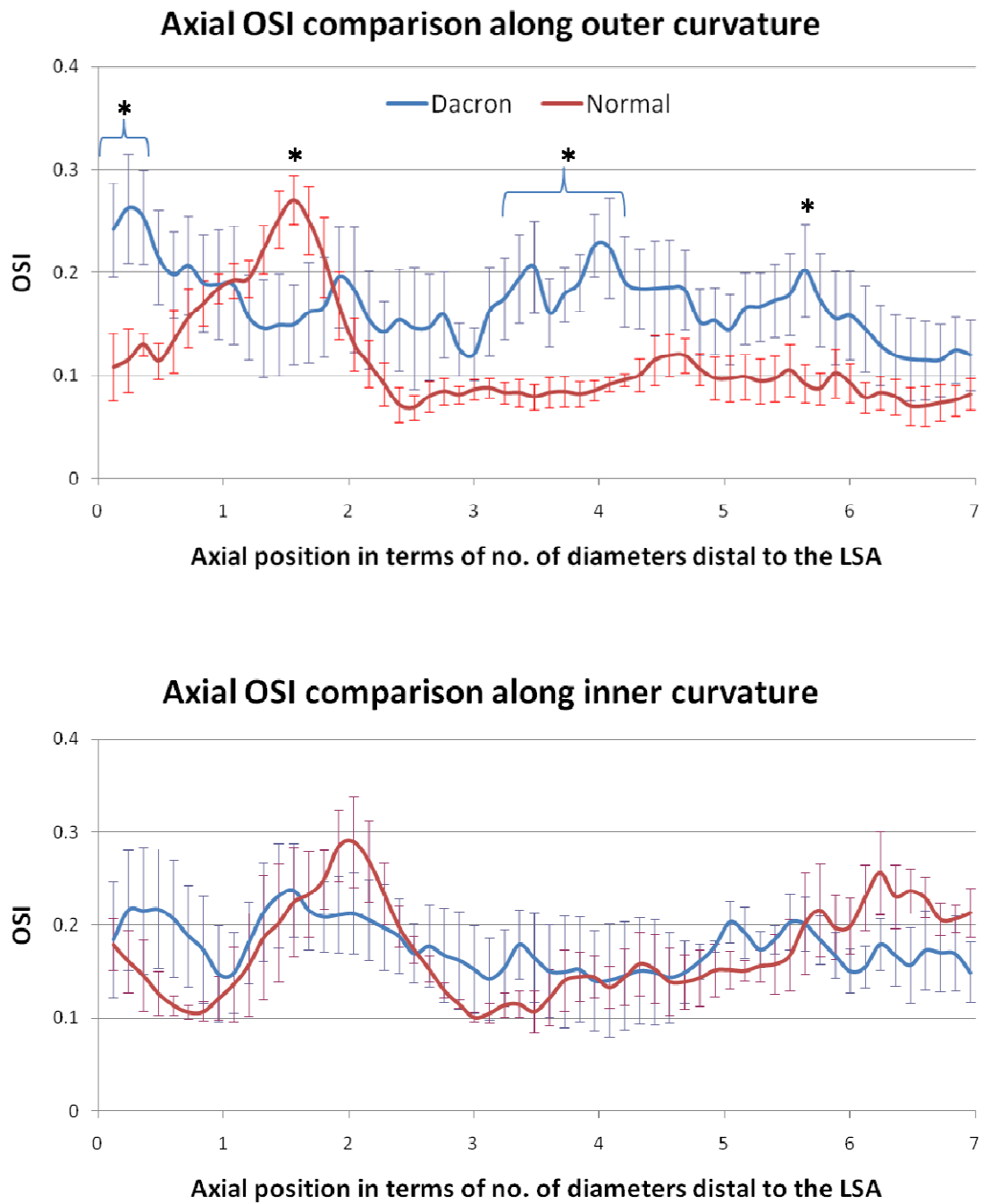
Figure 26. Ensemble-averaged axial OSI plots comparing Dacron patients with normal subjects along outer (top) and inner (below) curvature. * Statistically different from Normal subjects (P < 0.05). Data are expressed as mean ± SEM.

Axial OSI comparison along anatomic right curvature

Axial OSI comparison along anatomic left curvature
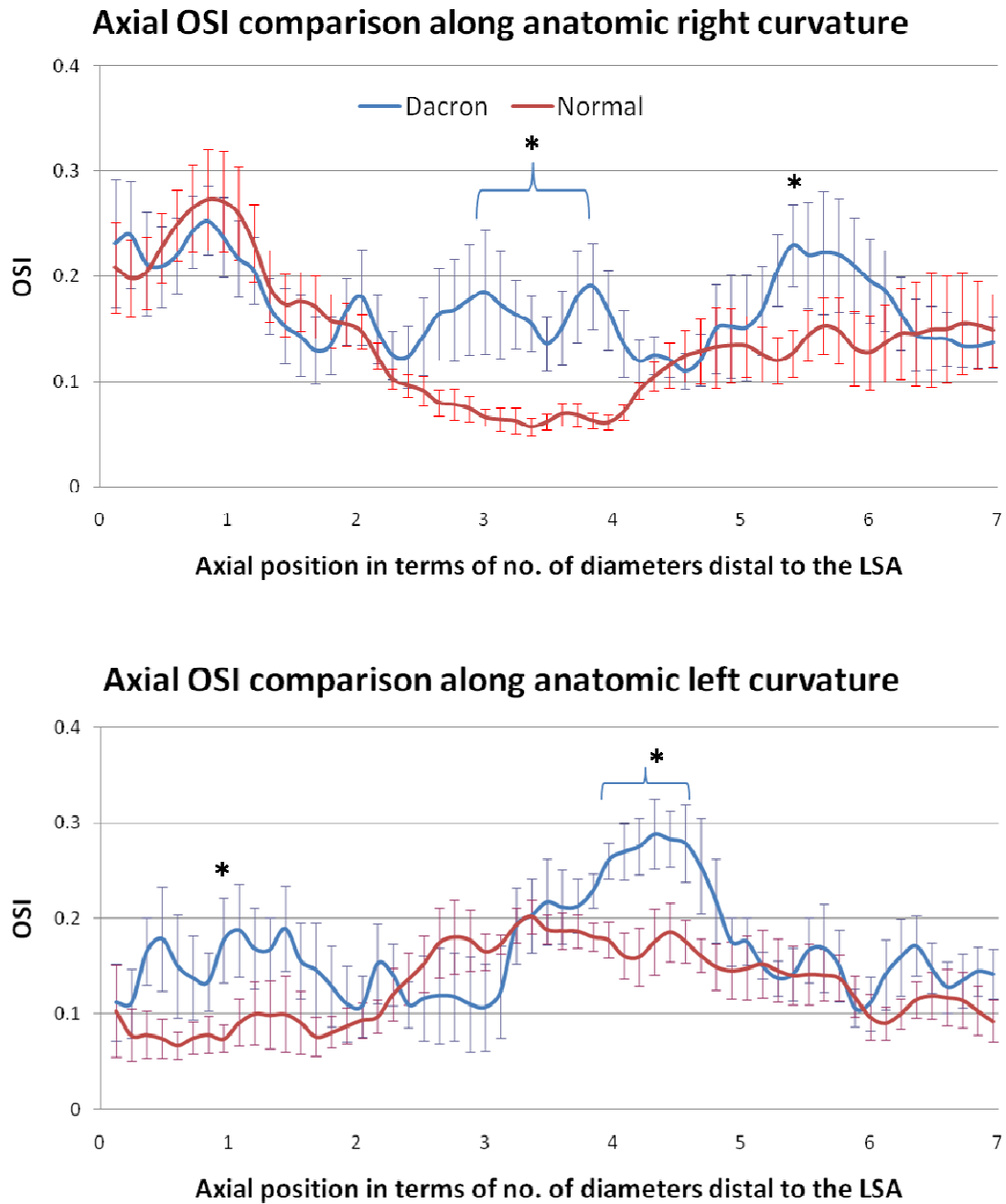
Figure 27. Ensemble-averaged axial OSI plots comparing Dacron patients with normal subjects along anatomic right (top) and anatomic left (below) curvature. * Statistically different from Normal subjects (P < 0.05). Data are expressed as mean ± SEM.

Figure 28 depicts the spatial location of circumferential quantification regions for each patient. TAWSS in these plots was also normalized by dividing by each patient's cardiac output. Circumferential plots are divided into 16 sectors of equal size that were then averaged similar to previous studies (Wentzel et al. 2005) to compare TAWSS and OSI between Dacron patients and Normal subjects. Figure 29 shows the division of the circumferential plot into 16 equal sectors with respect to their anatomic positions.
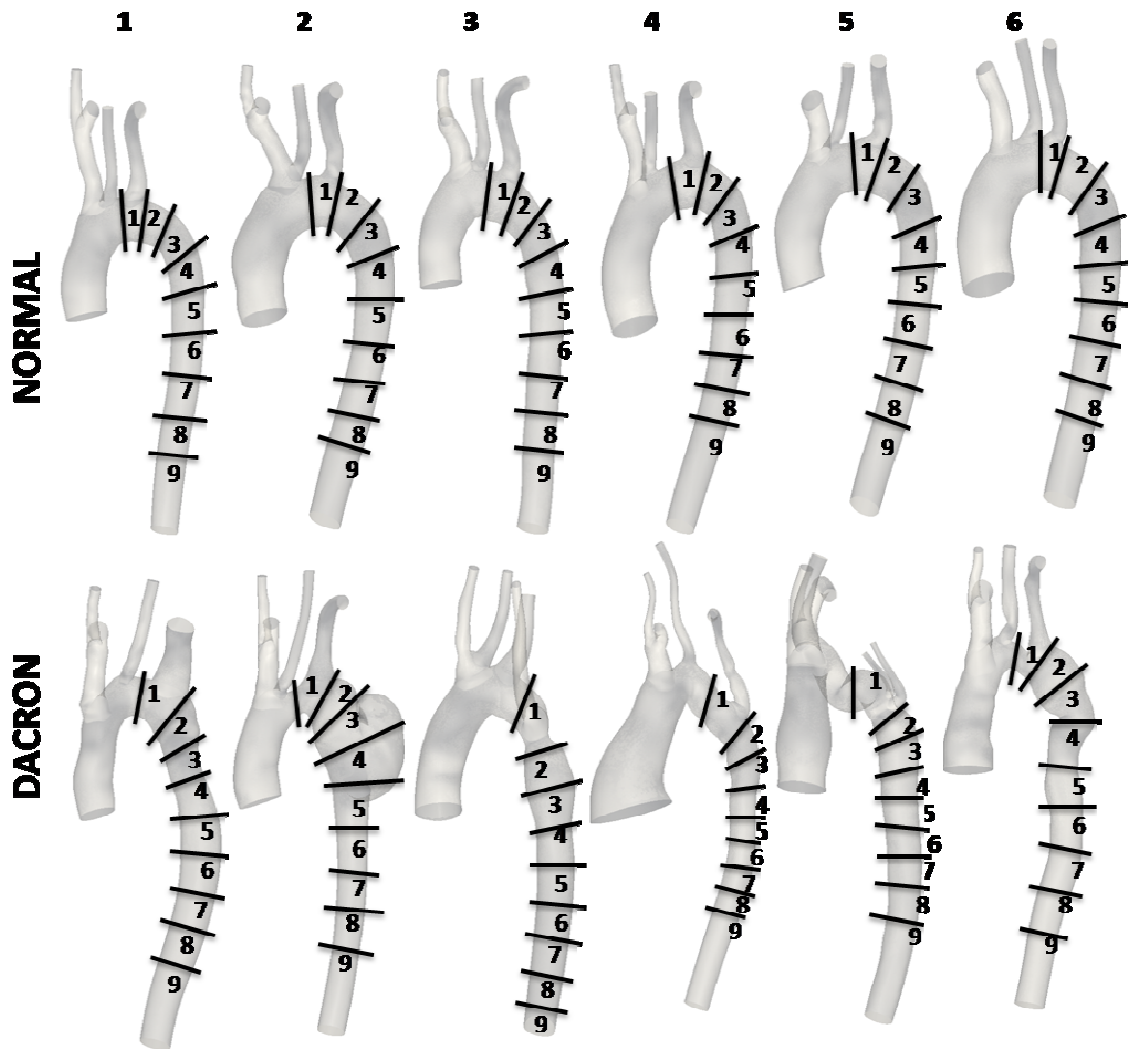
Figure 28. Schematic illustration of orthogonal locations along the aorta where circumferential TAWSS and OSI plots were quantified for each of the 6 Normal subjects (top row) and corresponding 6 Dacron patients (bottom row). Position 1 = transverse aortic arch, position 2 = just distal to the LSA, positions 3 to 9 = 1 to 7 descending aortic diameters distal to the LSA.
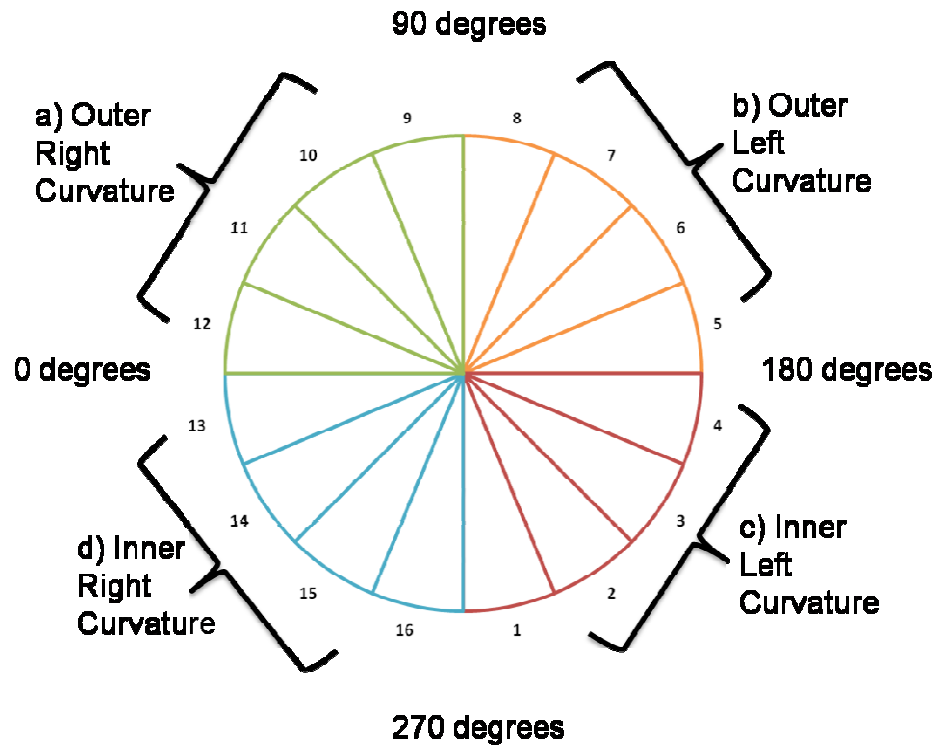
Figure 29. Schematic representation of how circumferential plots of TAWSS and OSI were quantified into 16 equal sectors with respect to anatomic positions.

Figures 30, 31 and 32 show circumferential distributions of TAWSS for Dacron patients and Normal subjects. Dacron subjects had higher TAWSS as compared to Normal subjects in nearly all circumferential sectors of the transverse arch (sector number 1 - 5, 10 – 13). Just distal to the LSA, TAWSS decreased significantly along the outer curvature and increased at sector 15 for Dacron patients with respect to Normal subjects. At 1 diameter and 3 diameters distal to the LSA, Dacron patients show reversing of TAWSS patterns with respect to Normal subjects. Dacron patients show higher TAWSS close to the anatomic right and outer curvatures at 1 diameter distal. Close to the anatomic left curvature, a significant increase in TAWSS is seen for Dacron patients at 3

diameters distal. Between 4, 5 and 7 diameters distal to LSA, no significant difference in TAWSS in Dacron patients and Normal subjects along the circumferential plots was seen in Figure 32. Stabilization of TAWSS is observed Normal subjects as well as Dacron patients beyond 4 diameters from the LSA, except at 6 diameters distal, where a significant decrease in TAWSS is seen close to the anatomic right and outer curvatures for Dacron patients.

Comparisons of OSI are shown in Figures 33, 34 and 35. Circumferential plot for OSI at the transverse arch show significantly low values of OSI along the anatomic inner right and inner left curvatures for the Dacron patients. Just distal to the LSA, decreased OSI along the inner right curvature and increased OSI at the outer and close to the anatomic left curvatures for the Dacron patients can be observed. At 1 diameter distal to the LSA, a significant increase in OSI is observed along almost the entire anatomic left curvature between sectors 1 to 7. The outer right curvature between sectors 9 to 12 demonstrates an increase in OSI too at 3 diameters distal to the LSA for the Dacron patients. As seen in Figure 35 no significant change in OSI between the Normal subjects and Dacron patients occurs from 4 diameters to 7 diameters distal.

Figure 30. Circumferential plots of TAWSS in each of the 16 sectors shown in Figure 29 for Normal subjects (red squares) and Dacron patients (blue diamonds) obtained in the transverse arch (top) and just distal to LSA (bottom). a = anatomic outer right curvature, b = anatomic outer left curvature, c = anatomic inner left curvature, d = anatomic inner right curvature. * Statistically different (p < 0.05) from Normal. Data are expressed as mean ± SEM.
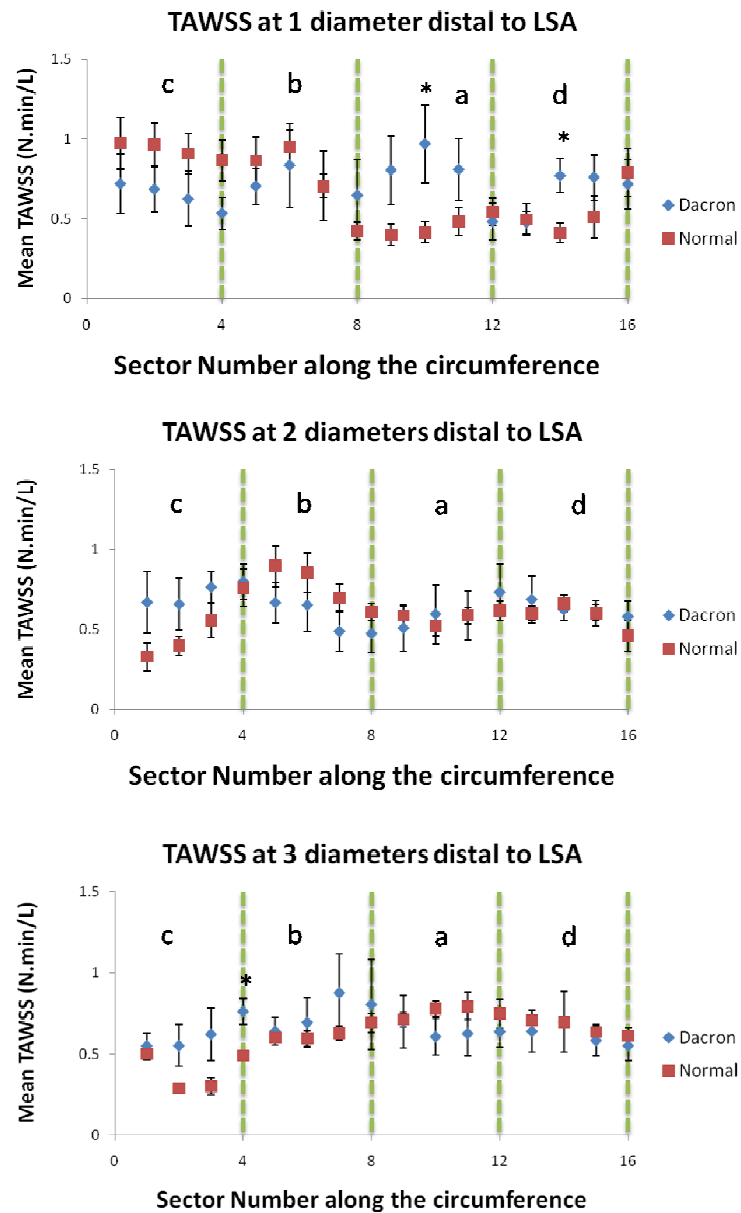
Figure 31. Circumferential plots of TAWSS in each of the 16 sectors shown in Figure 29 for Normal subjects (red squares) and Dacron patients (blue diamonds) obtained 1 (top), 2 (middle) and 3 (bottom) diameters distal to LSA. a = anatomic outer right curvature, b = anatomic outer left curvature, c = anatomic inner left curvature, d = anatomic inner right curvature. * Statistically different (p < 0.05) from Normal. Data are expressed as mean ± SEM.
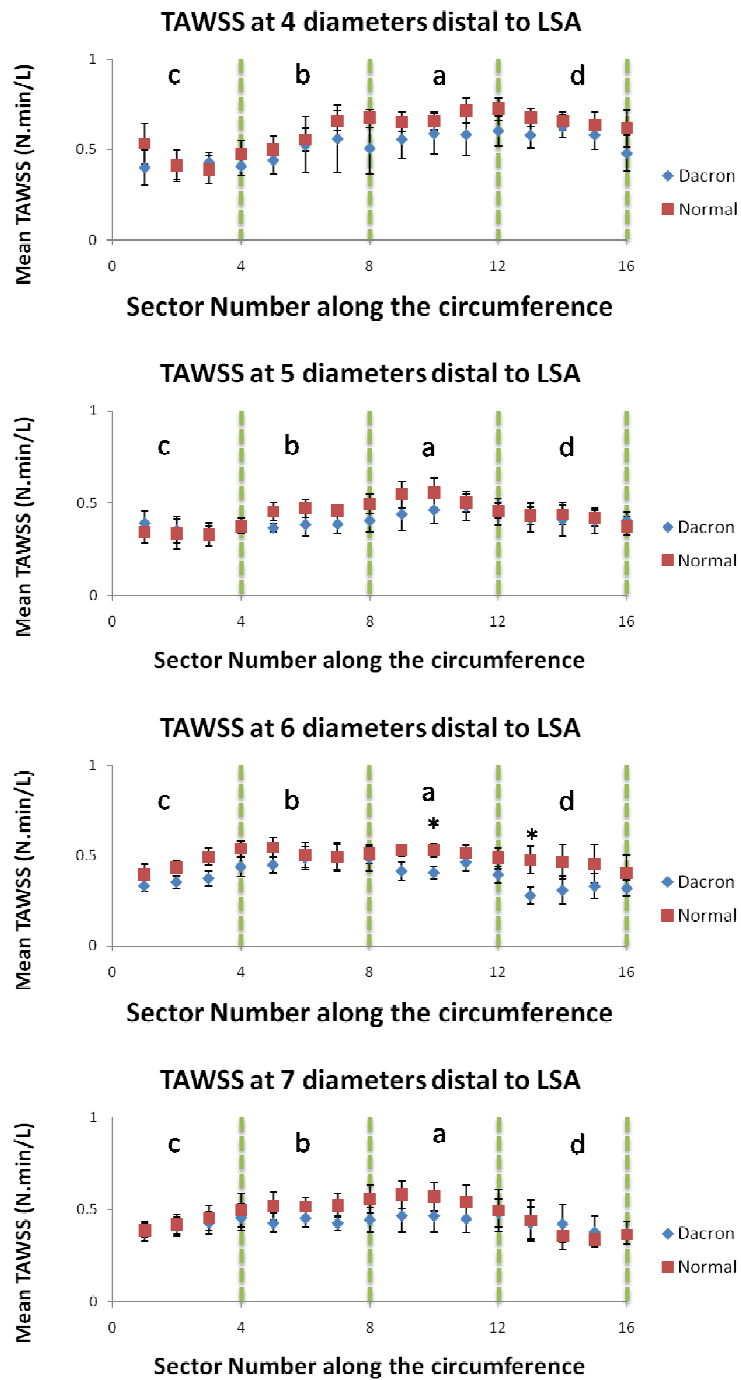
Figure 32. Circumferential plots of TAWSS in each of the 16 sectors shown in Figure 29 for Normal subjects (red squares) and Dacron patients (blue diamonds) obtained 4 -7 (top to bottom) diameters distal to LSA. a = anatomic outer right curvature, b = anatomic outer left curvature, c = anatomic inner left curvature, d = anatomic inner right curvature. * Statistically different (p < 0.05) from Normal. Data are expressed as mean ± SEM.
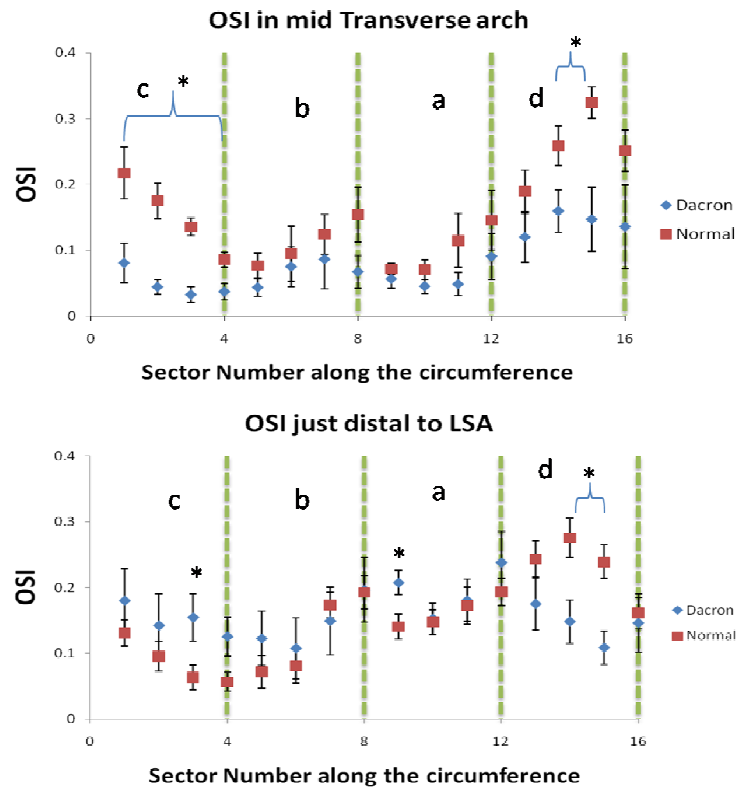
Figure 33. Circumferential plots of OSI in each of the 16 sectors shown in Figure 29 for Normal subjects (red squares) and Dacron patients (blue diamonds) obtained in the transverse arch (top) and just distal to LSA (bottom). a = anatomic outer right curvature, b = anatomic outer left curvature, c = anatomic inner left curvature, d = anatomic inner right curvature. * Statistically different (p < 0.05) from Normal. Data are expressed as mean ± SEM.
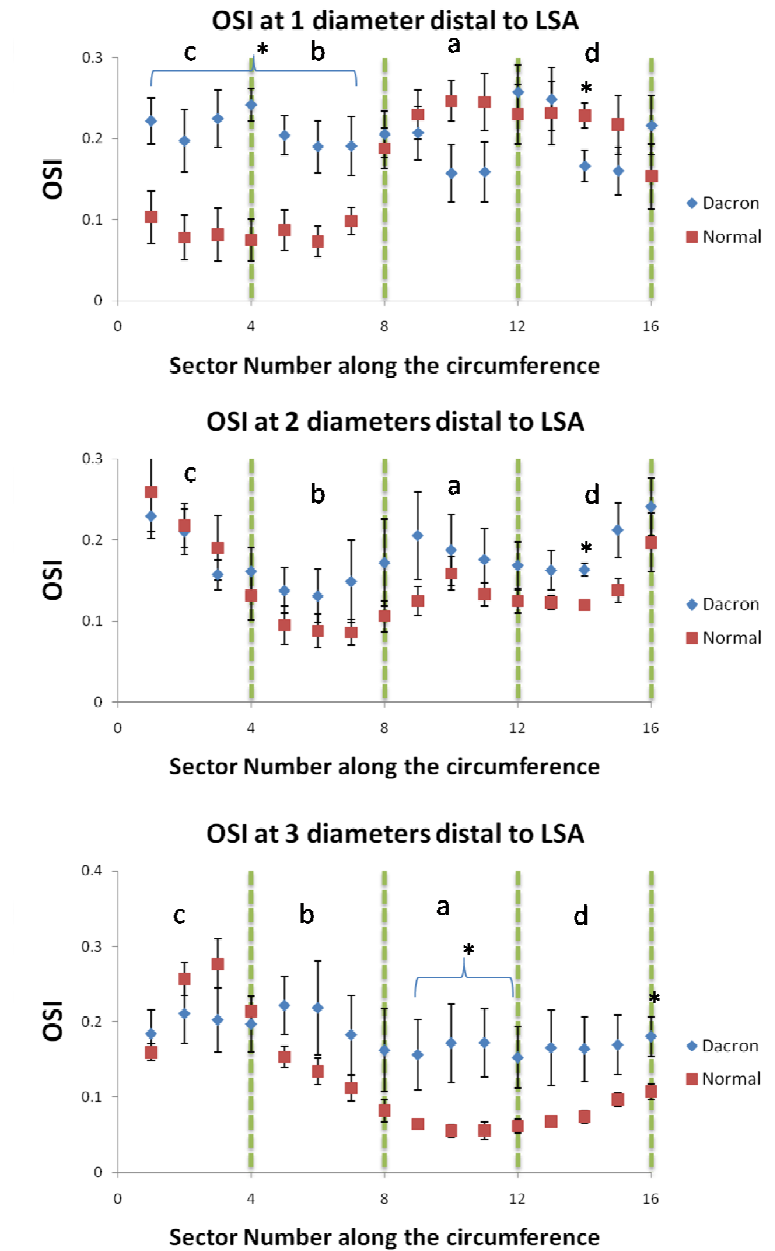
Figure 34. Circumferential plots of OSI in each of the 16 sectors shown in Figure 29 for Normal subjects (red squares) and Dacron patients (blue diamonds) obtained 1 (top), 2 (middle) and 3 (bottom) diameters distal to LSA. a = anatomic outer right curvature, b = anatomic outer left curvature, c = anatomic inner left curvature, d = anatomic inner right curvature. * Statistically different (p < 0.05) from Normal. Data are expressed as mean ± SEM.
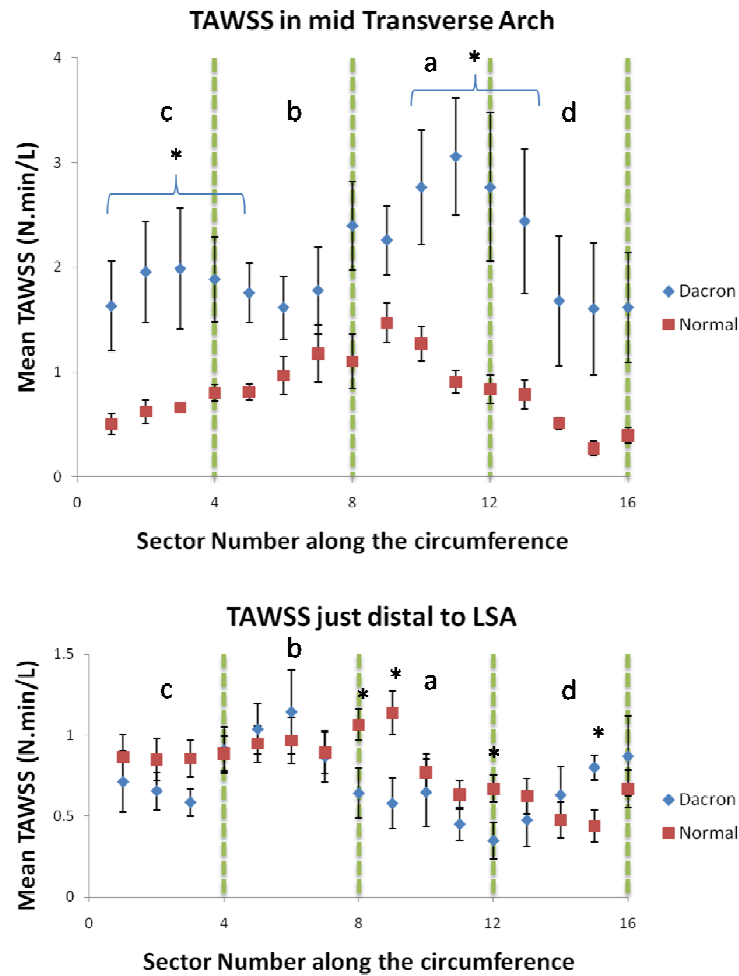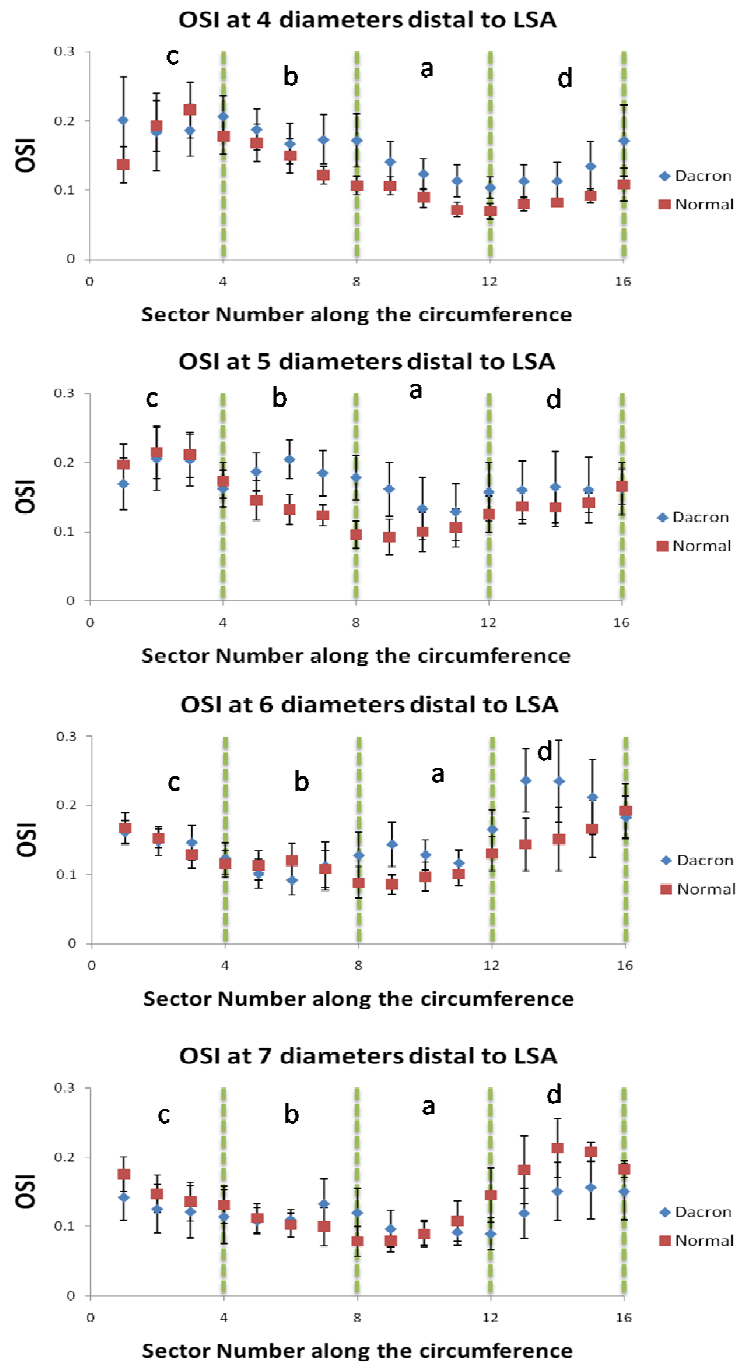
Figure 35. Circumferential plots of OSI in each of the 16 sectors shown in Figure 29 for Normal subjects (red squares) and Dacron patients (blue diamonds) obtained 4-7 (top to bottom) diameters distal to LSA. a = anatomic outer right curvature, b = anatomic outer left curvature, c = anatomic inner left curvature, d = anatomic inner right curvature. * Statistically different (p < 0.05) from Normal. Data are expressed as mean ± SEM.

Chapter 4 – Discussion

4.1. Review of hypothesis and specific aims

Parks et al reported a 51% incidence of aneurysms in CoA patients treated by Dacron patch aortoplasty in their follow up study in 1995 (Parks et al. 1995) and aneurysm formation has been seen as a long term post surgical effect after Dacron patch repair (Hehrlein et al. 1986; Nagano et al. 2007; Roth et al. 2002; Walhout et al. 2003). The current investigation is strongly motivated by the desire to further understand the potential impact of local hemodynamic alterations caused by this repair type and thus tested the hypothesis that repair of coarctation through Dacron patch aortoplasty causes alterations in vessel wall geometry, blood flow, blood velocity pattern, temporal WSS patterns, TAWSS and OSI patterns in the thoracic aorta. We aimed to quantify and characterize hemodynamics in six CoA patients treated with Dacron patch aortoplasty and in six corresponding age and gender matched normal subjects as well as compare the severity in local alterations of TAWSS and OSI indices between the two populations.

4.2. Summary of findings from the current investigation

To our knowledge, the current investigation is the first to elucidate detailed patterns of WSS and OSI in the thoracic aorta for any cohort of patients, Normal or otherwise, using patient-specific CFD modeling. Importantly, the inner curvature of the luminal surface within the transverse arch appears to be most susceptible to adverse

TAWSS and OSI and this region of susceptibility proceeds in a left-handed manner from 1-5 diameters distal to the LSA until TAWSS and OSI are relatively uniform around the circumference of the vessel. While there were several locations of significant difference between Normal and Dacron simulations, the CoA patients did not have a significantly greater percentage of the lumen surface exposed to low TAWSS. Similarly, the amount of the luminal surface distal to the LSA subjected to high OSI was similar between investigational groups, but there were a substantial number of locations where Dacron patients exhibited flow separation, particularly 4 to 5 diameters distal to the LSA. These observed differences in WSS indices between Normal subjects and CoA patients previously treated by Dacron aortoplasty can be attributed to blood flow velocity patterns resulting from vascular geometry and distributions of blood flow to arteries of the head and neck that has ensued since their correction.

4.3 Applicability of current findings to previous studies

Blood flow velocity streamlines obtained from the current CFD modeling results are consistent with velocity results obtained in normal subjects as elegantly quantified by Kilner et al. (Kilner et al. 1993) in their study using 3D MRI. Specifically, during early systole velocity streamlines were mainly axial in nature and fully attached, with secondary right-handed helical flow developing during the mid-to-late systole in all normal subjects. At early systole velocity streamlines near the inner curvature of the aorta demonstrated higher magnitude and at mid-to-late systole the velocity streamlines on the outer walls demonstrated higher magnitude. The current results demonstrated a single

concentrated region of flow separation along the inner curvature of the thoracic aorta at the level of the ductus arteriosus where Kilner et al. demonstrated right-handed helical flow transitions into left-handed but more axially oriented flow. These helical flow patterns seen in the currently study and demonstrated by Kilner et al. have also been observed by Wentzel et al. (Wentzel et al. 2005) in their study using PCMRI in the human thoracic aorta to derive WSS distributions along the walls. However, the WSS values included in this previous report were determined purely from velocity values obtained during imaging and thus the closeness in location at which near-wall velocity vectors were determined may have greatly impacted reported values. Previous studies by Frydrychowicz et al (Frydrychowicz et al. 2008) also made use of 3D MRI, but to study blood flow patterns in the thoracic aorta of surgically repaired coarctation patients. They found re-circulating flow in the aneurysm of the patients similar to those presented here for patients 2 and 6. Thus, results from the current investigation confirm and extend those in these previous reports by quantifying and characterizing the impact of these flow patterns on indices of WSS thought to contribute to long-term morbidity.

4.4. Potential Limitations

The current results should be interpreted with the constraints of several potential limitations. The Dacron patch aortoplasty patient population investigated was very heterogeneous with various vascular morphologies and subsequent changes in hemodynamics and may not necessarily reflect alterations that would be observed for the overall patient population of patients that underwent Dacron repair. This may be due to

the fact that data for the current investigation was obtained from CoA patients treated with Dacron patch aortoplasty that had returned to the clinics and it is perhaps reasonable to infer that these patients may represent a sampling of Dacron patch patients with a less favorable outcome as compared to those with the same surgery that did not require clinical follow-up and thus were not included here. The bicuspid aortic valve seen in most CoA patients, or the tricuspid valves in some of the patients used in the present investigation were not incorporated into the CFD models. Instead parabolic blood flow velocity profiles were implemented as the inflow boundary condition. The difference in flow profiles through bicuspid or tricuspid aortic valves as compared to a parabolic inlet might not results in true patterns of WSS and OSI in the ascending aorta. These regions were therefore omitted during quantification of results in the current investigation.

All patient specific solid models for running CFD simulations were created by a single user. While the process for creating patient-specific CFD models described here has been utilized by many investigators and makes attempts to standardize parameters selected during the model creation process, vascular geometries may have been modestly different for a different user and these differences have been previously quantified (Steinman 2002). Distributions of blood flow to arteries of the head and neck were not available for Normal patients in the current investigation and the ascending aortic inflow waveform was estimated from previous literature for a single normal patient. It is therefore possible, that these estimates may have differed from the actual physiologic values had they been measured at the conclusion of the clinical imaging session.

A constant and assumed viscosity was used throughout the CFD model for all the patients since rheological data was not available. The simulations were also performed using a rigid wall assumption. Thus, no elastic modulus was assigned to the blood vessel walls or the Dacron patch and the difference in the stiffness of the patch material and the compliant aorta are not taken into account. This decision was made largely because the exact locations of Dacron patch repair were not identifiable.

4.5. Future directions

Surgically repaired coarctation patients in future studies should have homogeneous post-surgical geometry for a better overall comparison. Elastic modulus should be incorporated in the model, making the vessel walls deformable to take into account the rigid nature of the patch. The sample size may yield better results if increased. Additionally, inclusion of valve morphology should be done if possible in order to obtain more realistic flow patterns in the ascending aorta.

Localized quantification of hemodynamic indices in the thoracic aorta in normal subjects provides a useful screening tool for other diseases of the thoracic aorta. In the future, other patient populations with diseases of the thoracic aorta could be compared to normal subjects to identify areas of hemodynamic vulnerability. CFD simulations along with imaging techniques could be used a post-surgical follow up tool for patients.

BIBLIOGRAPHY

Ala-Kulju, K. and L. Heikkinen. 1989. Aneurysms after patch graft aortoplasty for coarctation of the aorta: Long-term results of surgical management. *Ann Thorac Surg* 47, no. 6: 853-6.

Appleyard, R. F. and L. R. Sauvage. 1986. Haemodynamic consequences of arterial replacement with a synthetic graft. *Cardiovasc Res* 20, no. 1: 26-35.

Bauernschmitt, R., S. Schulz, A. Schwarzhaupt, U. Kiencke, C. F. Vahl, R. Lange, and S. Hagl. 1999. Simulation of arterial hemodynamics after partial prosthetic replacement of the aorta. *Ann Thorac Surg* 67, no. 3: 676-82.

Bernstein, M. A., X. J. Zhou, J. A. Polzin, K. F. King, A. Ganin, N. J. Pelc, and G. H. Glover. 1998. Concomitant gradient terms in phase contrast mr: Analysis and correction. *Magn Reson Med* 39: 300–308.

Cheng, C. P., R. J. Herfkens, A. L. Lightner, C. A. Taylor, and J. A. Feinstein. 2004. Blood flow conditions in the proximal pulmonary arteries and vena cavae: Healthy children during upright cycling exercise. *Am J Physiol Heart Circ Physiol* 287, no. 2: H921-6.

Cohen, M., V. Fuster, P. M. Steele, D. Driscoll, and D. C. McGoon. 1989. Coarctation of the aorta. Long-term follow-up and prediction of outcome after surgical correction. *Circulation* 80, no. 4: 840-5.

DeSanto, A., R. G. Bills, H. King, B. Waller, and J. W. Brown. 1987. Pathogenesis of aneurysm formation opposite prosthetic patches used for coarctation repair. An experimental study. *J Thorac Cardiovasc Surg* 94, no. 5: 720-3.

Drizd, T., A. L. Dannenberg, and A. Engel. 1986. Blood pressure levels in persons 18-74 years of age in 1976-80, and trends in blood pressure from 1960 to 1980 in the united states. *Vital Health Stat 11*, no. 234: 1-68.

Figueroa, C. A., I. E. Vignon-Clementel, K. E. Jansen, T. J. R. Hughes, and C. A. Taylor. 2006. A coupled momentum method for modeling blood flow in three-dimensional deformable arteries. *Comput Methods Appl Mech Eng* 195: 5685-5706.

Frydrychowicz, A., R. Arnold, D. Hirtler, C. Schlensak, A. F. Stalder, J. Hennig, M. Langer, and M. Markl. 2008. Multidirectional flow analysis by cardiovascular magnetic resonance in aneurysm development following repair of aortic coarctation. *J Cardiovasc Magn Reson* 10, no. 1: 30.

Hehrlein, F. W., J. Mulch, H. W. Rautenburg, M. Schlepper, and H. H. Scheld. 1986. Incidence and pathogenesis of late aneurysms after patch graft aortoplasty for coarctation. *J Thorac Cardiovasc Surg* 92, no. 2: 226-30.

Heiberg, Einar. 2007. Validation of free software for automated vessel delineation and mri flow analysis
Journal of Cardiovascular Magnetic Resonance 9, no. 2: 375-376.

Heikkinen, L., H. Sariola, J. Salo, and K. Ala-Kulju. 1990. Morphological and histopathological aspects of aneurysms after patch aortoplasty for coarctation. *Ann Thorac Surg* 50, no. 6: 946-8.

Hoimyr, H., T. D. Christensen, K. Emmertsen, S. P. Johnsen, A. Riis, O. K. Hansen, and V. E. Hjortdal. 2006. Surgical repair of coarctation of the aorta: Up to 40 years of follow-up. *Eur J Cardiothorac Surg* 30, no. 6: 910-6.

Katritsis, D., L. Kaiktsis, A. Chaniotis, J. Pantos, E. P. Efstathopoulos, and V. Marmarelis. 2007. Wall shear stress: Theoretical considerations and methods of measurement. *Prog Cardiovasc Dis* 49, no. 5: 307-29.

Kilner, P. J., G. Z. Yang, R. H. Mohiaddin, D. N. Firmin, and D. B. Longmore. 1993. Helical and retrograde secondary flow patterns in the aortic arch studied by three-directional magnetic resonance velocity mapping. *Circulation* 88, no. 5 Pt 1: 2235-47.

Kim, S. Y., T. J. Hinkamp, W. R. Jacobs, R. C. Lichtenberg, H. Posniak, and R. Pifarre. 1995. Effect of an inelastic aortic synthetic vascular graft on exercise hemodynamics. *Ann Thorac Surg* 59, no. 4: 981-9.

Laskey, W. K., H. G. Parker, V. A. Ferrari, W. G. Kussmaul, and A. Noordergraaf. 1990. Estimation of total systemic arterial compliance in humans. *J Appl Physiol* 69, no. 1: 112-9.

May, LE. 2005. *Pediatric heart surgery: A ready reference for professionals*. Milwaukee, WI: Maxishare.

McGiffin, D. C., P. B. McGiffin, A. J. Galbraith, and R. B. Cross. 1992. Aortic wall stress profile after repair of coarctation of the aorta. It is related to subsequent true aneurysm formation? *J Thorac Cardiovasc Surg* 104, no. 4: 924-31.

Michael Madrzak, PA-C. 2008. Congenital heart disease an introduction. In *Lecture Notes in Cardiopulmonary Mechanics*: Children's Hospital of WI, Herma Heart Center.

Mirnajafi, A., J. Raymer, M. J. Scott, and M. S. Sacks. 2005. The effects of collagen fiber orientation on the flexural properties of pericardial heterograft biomaterials. *Biomaterials* 26, no. 7: 795-804.

Murgo, J. P., N. Westerhof, J. P. Giolma, and S. A. Altobelli. 1981. Effects of exercise on aortic input impedance and pressure wave forms in normal humans. *Circ Res* 48, no. 3: 334-43.

Nagano, N., R. Cartier, T. Zigras, R. Mongrain, and R. L. Leask. 2007. Mechanical properties and microscopic findings of a dacron graft explanted 27 years after coarctation repair. *J Thorac Cardiovasc Surg* 134, no. 6: 1577-8.

Nichols DG, Cameron DE, Greeley WJ. 2006. *Critical heart disease in infants and children*. Philadelphia, Pa: Mosby.

Nichols, W. W. and M. F. O'Rourke. 2005. *Mcdonald's blood flow in arteries: Theoretical, experimental and clinical principles*. New York: Hodder Arnold.

O'Rourke, M. F. and M. E. Safar. 2005. Relationship between aortic stiffening and microvascular disease in brain and kidney: Cause and logic of therapy. *Hypertension* 46, no. 1: 200-4.

Omeje IC, Poruban R, Sagat M, Nosal M, Hraska V. 2004. Surgical treatment of aortic coarctation. *Images Pediatr Cardiol* 19: 18-28.

Park, MK. 2003. *The pediatric cardiology handbook*. St Louis, Mo: Mosby.

Parks, W. J., T. D. Ngo, W. H. Plauth, Jr., E. R. Bank, S. K. Sheppard, R. I. Pettigrew, and W. H. Williams. 1995. Incidence of aneurysm formation after dacron patch aortoplasty repair for coarctation of the aorta: Long-term results and assessment utilizing magnetic resonance angiography with three-dimensional surface rendering. *J Am Coll Cardiol* 26, no. 1: 266-71.

Pekkan, K., D. Frakes, D. De Zelicourt, C. W. Lucas, W. J. Parks, and A. P. Yoganathan. 2005. Coupling pediatric ventricle assist devices to the fontan circulation: Simulations with a lumped-parameter model. *Asaio J* 51, no. 5: 618-28.

Pelc, L. R., N. J. Pelc, S. C. Rayhill, L. J. Castro, G. H. Glover, R. J. Herfkens, D. C. Miller, and R. B. Jeffrey. 1992. Arterial and venous blood flow: Noninvasive quantitation with mr imaging. *Radiology* 185: 809–812.

Pizarro, C. and M. R. De Leval. 1998. Surgical variations and flow dynamics in cavopulmonary connections: A historical review. *Semin Thorac Cardiovasc Surg Pediatr Card Surg Annu* 1: 53-60.

Prakash, S. and C. R. Ethier. 2001. Requirements for mesh resolution in 3d computational hemodynamics. *J Biomech Eng* 123, no. 2: 134-44.

Rees, S., J. Somerville, C. Ward, J. Martinez, R. H. Mohiaddin, R. Underwood, and D. B. Longmore. 1989. Coarctation of the aorta: Mr imaging in late postoperative assessment. *Radiology* 173, no. 2: 499-502.

Roth, M., P. Lemke, M. Schonburg, W. P. Klovekorn, and E. P. Bauer. 2002. Aneurysm formation after patch aortoplasty repair (vossschulte): Reoperation in adults with and without hypothermic circulatory arrest. *Ann Thorac Surg* 74, no. 6: 2047-50.

Rubin, Raphael. 2008. *Rubin's pathology: Clinicopathologic foundations of medicince*. Philadelphia, Pa: Williams & Williams.

Schuster, S. R. and R. E. Gross. 1962. Surgery for coarctation of the aorta. A review of 500 cases. *J Thorac Cardiovasc Surg* 43: 54-70.

Seear, M., S. Webber, and J. Leblanc. 1994. Descending aortic blood flow velocity as a noninvasive measure of cardiac output in children. *Pediatr Cardiol* 15, no. 4: 178-83.

Shi, Q., M. H. Wu, Y. Onuki, R. Ghali, G. C. Hunter, K. H. Johansen, and L. R. Sauvage. 1997. Endothelium on the flow surface of human aortic dacron vascular grafts. *J Vasc Surg* 25, no. 4: 736-42.

Smaill, B. H., D. C. McGiffin, I. J. Legrice, A. A. Young, P. J. Hunter, and A. J. Galbraith. 2000. The effect of synthetic patch repair of coarctation on regional deformation of the aortic wall. *J Thorac Cardiovasc Surg* 120, no. 6: 1053-63.

Socci, L., F. Gervaso, F. Migliavacca, G. Pennati, G. Dubini, L. Ait-Ali, P. Festa, F. Amoretti, L. Scebba, and V. S. Luisi. 2005. Computational fluid dynamics in a model of the total cavopulmonary connection reconstructed using magnetic resonance images. *Cardiol Young* 15 Suppl 3: 61-7.

Steinman, D. A. 2002. Image-based computational fluid dynamics modeling in realistic arterial geometries. *Ann Biomed Eng* 30, no. 4: 483-97.

Steinman, D. A. and C. A. Taylor. 2005. Flow imaging and computing: Large artery hemodynamics. *Ann Biomed Eng* 33, no. 12: 1704-9.

Stergiopulos, N., P. Segers, and N. Westerhof. 1999. Use of pulse pressure method for estimating total arterial compliance in vivo. *Am J Physiol Heart Circ Physiol* 276, no. 45: H424-8.

Stergiopulos, N., D. F. Young, and T. R. Rogge. 1992. Computer simulation of arterial flow with applications to arterial and aortic stenoses. *J Biomech* 25, no. 12: 1477-88.

Suo, J., D. E. Ferrara, D. Sorescu, R. E. Guldberg, W. R. Taylor, and D. P. Giddens. 2007. Hemodynamic shear stresses in mouse aortas: Implications for atherogenesis. *Arterioscler Thromb Vasc Biol* 27, no. 2: 346-51.

Tang, B. T., C. P. Cheng, M. T. Draney, N. M. Wilson, P. S. Tsao, R. J. Herfkens, and C. A. Taylor. 2006. Abdominal aortic hemodynamics in young healthy adults at rest and during lower limb exercise: Quantification using image-based computer modeling. *Am J Physiol Heart Circ Physiol* 291, no. 2: H668-76.

Vignon-Clementel, I. E., C. A. Figueroa, K. E. Jansen, and C. A. Taylor. 2006. Outflow boundary conditions for three-dimensional finite element modeling of blood flow and pressure in arteries. *Comput Methods Appl Mech Eng* 195: 3776-96.

von Kodolitsch, Y., M. A. Aydin, D. H. Koschyk, R. Loose, I. Schalwat, M. Karck, J. Cremer, A. Haverich, J. Berger, T. Meinertz, and C. A. Nienaber. 2002. Predictors of aneurysmal

formation after surgical correction of aortic coarctation. *J Am Coll Cardiol* 39, no. 4: 617-24.

Vossschulte, K. 1957. [plastic surgery of the isthmus in aortic isthmus stenosis.]. *Thoraxchirurgie* 4, no. 5: 443-50.

Walhout, R. J., J. C. Lekkerkerker, G. H. Oron, F. J. Hitchcock, E. J. Meijboom, and G. B. Bennink. 2003. Comparison of polytetrafluoroethylene patch aortoplasty and end-to-end anastomosis for coarctation of the aorta. *J Thorac Cardiovasc Surg* 126, no. 2: 521-8.

Wang, K. C., R. W. Dutton, and C. A. Taylor. 1999. Level sets for vascular model construction in computational hemodynamics. *IEEE Engineering in Medicine and Biology* 18, no. 6: 33-39.

Wentzel, J. J., R. Corti, Z. A. Fayad, P. Wisdom, F. Macaluso, M. O. Winkelman, V. Fuster, and J. J. Badimon. 2005. Does shear stress modulate both plaque progression and regression in the thoracic aorta? Human study using serial magnetic resonance imaging. *J Am Coll Cardiol* 45, no. 6: 846-54.

Westerhof, N., N. Stergiopulos, and M. I. M. Noble. 2005. *Snapshots of hemodynamics an aid for clinical research and graduate education*. New York: Springer.

Wilson, N., K. Wang, R. Dutton, and C. A. Taylor. 2001. A software framework for creating patient specific geometric models from medical imaging data for simulation based medical planning of vascular surgery. *Lect Notes Comput Sci* 2208: 449-456.

Wilson, S. E., R. Krug, G. Mueller, and L. Wilson. 1997. Late disruption of dacron aortic grafts. *Ann Vasc Surg* 11, no. 4: 383-6.

Zamir, M., P. Sinclair, and T. H. Wonnacott. 1992. Relation between diameter and flow in major branches of the arch of the aorta. *J Biomech* 25, no. 11: 1303-10.